QUANTITATIVE VISUALIZATION OF CARBON DIOXIDE GAS TRANSFER AT A TURBULENT FREE SURFACE

A Thesis

Presented to the Faculty of the Graduate School

of Cornell University

In Partial Fulfillment of the Requirements for the Degree of

Master of Science

by

Evan Variano

August 2005

ABSTRACT

We study the aqueous-phase side of the transfer of carbon dioxide gas across an air-water interface. Quantitative imaging techniques are used to directly visualize the physical processes which determine the average gas transfer rate. The interface is a free surface in the absence of mean shear, with turbulence generated on the water side, well away from the free surface, which then transports itself to the free surface. This turbulence is generated far beneath the free surface by an array of upward-pointing synthetic jets which are each driven according to independent random time series. We show that this method of turbulence generation is superior to the traditional grid-stirred tank in that it exhibits weaker mean secondary flows.

Using Laser Induced Fluorescence (LIF) and Particle Image Velocimetry (PIV) we measure simultaneous concentration and velocity fields, respectively. These are measured in planar fields perpendicular to and intersecting the free surface. From these we calculate turbulent statistics of interest. Namely, the vertical profiles of mean and fluctuating velocity magnitudes, momentum dissipation rate, spatial power spectra for velocity and concentration, and the turbulent mass flux.

Examination of the turbulent mass flux field reveals that downward-traveling fluid, which leaves the concentration boundary layer at the surface and enters the bulk, is responsible for the majority of the gas transfer. This is in contrast to the commonly held view that upward-traveling fluid from the bulk dominates gas transfer. The spectrum of the turbulent mass flux field is nearly flat, showing that motions of all sizes in the inertial subrange contribute equally to the mass transfer. This resolves the longstanding question about which size eddies are responsible for gas transfer.

BIOGRAPHICAL SKETCH

The author was born in Ithaca, New York. There he attended Central Elementary School. The alternative education strategy used there was a good foundation for the development of the creativity and self-motivation needed for graduate work. Thus thanks go to the teachers and administrators who had the dedication and daring to create such a learning environment. After graduating public high school in southern New York state, the author attended Princeton University. Earning a BA in physics there, he joined Marakon Associates, an international consulting firm specializing in corporate strategy and finance. Thereafter he worked at the Queensland Australia branch of Amnesty International, developing their educational outreach materials to help high school students engage with human rights issues. Returning to Ithaca, the author rediscovered some of the many joys of that amazing corner of the world. While many of these are obvious, there are several that other graduate students may not readily find. He found the Willard Way overlook by following University Ave down the hill past Alice Cook House and crossing Stewart Ave, making his next right, and then a quick left, onto Willard Way. At the end of this street he found a great view of Ithaca Falls from above. He also enjoyed hiking Coy Glen, aptly named, by taking Seneca Street downhill and then through town. At its very end, he made a left onto Route 13A, then a right onto Coy Glen Road, then a left onto Elm Street Ext. About a mile up, there was a wide shoulder on the road with room to park, on the left just past a bridge that goes over the glen. He needed waterproof sandals to hike the glen, as some parts had to be waded. In winter time he enjoyed sledding through the old cemetery between University and Stewart Avenues. The Northwest corner of the cemetery has several crypts, between which were three nicely terraced runs. The author thought that the biographical tense was hilarious.

This work is dedicated to Ithaca – its waterfalls and creeks have provided inspiration, its people have provided more than imaginable.

ACKNOWLEDGMENTS

Sincere thanks go to the following for the contribution of time and resources to this project: Bill Asher, Jim Bisogni, Qian Liao, Lance Collins, John Powers, Willem Van de Water, Allie King, Monroe Weber Shirk, Tim Brock, Paul Charles, Gustavo Zarruk, Khaled al Banaa, PJ Rusello, In-Mei Sou, Lee Virtue, Eberhard Bodenschatz, Alice Crawford, Nicolas Mordant, Anders Andersen.

For providing an *ad hoc* writers retreat for the creation of this written document I thank the Swarthmore College Women's Ultimate Frisbee Team – Go Warmothers!

This work was supported by: NSF CAREER Grant CTS-0093794, NSF IGERT Site Grant DGE-9870631, and NSF GK-12 Site Grant 0231913. Any opinions, findings, and conclusions or recommendations are those of the author(s) and do not necessarily reflect the views of the National Science Foundation.

TABLE OF CONTENTS

LIST OF FIGURES

LIST OF TABLES

CHAPTER 1

BACKGROUND

1.1 Introduction

Direct measurement of instantaneous turbulent scalar flux across a boundary is relevant to many systems of interest in environmental fluid mechanics. Scalars of interest include heat, oxygen, carbon dioxide, and sediment. The boundary of interest can be a free surface or no-slip. The flow near the boundary can exhibit mean shear or be shear-free. This work considers the transfer of CO_2 across a shear-free free surface boundary, which is of direct relevance to questions of the global carbon budget and thus to global climate change. In addition, elements of this work can be extended to the related systems described above.

On both sides of an air-water interface, turbulent eddies act to thin the concentration boundary layer (CBL), making a steeper concentration gradient and thus enhancing the rate of molecular diffusion which is ultimately responsible for the transfer. At an air-water boundary, the rate of CO_2 gas transfer depends strongly on the strength of the water-side turbulence (Asher & Wanninkhof 1998). Here we directly measure the water-side turbulence and its effect on transfer. We investigate the fundamental mechanisms by which a turbulent eddy effects the CBL to enhance transfer. This physics is relevant to transfer in either direction (invasion or evasion), though the case studied here is strong invasion, *i.e.* pure CO_2 gas crossing a boundary into CO_2-depleted water.

The turbulence responsible for increasing air-water gas transfer is often generated at the surface, through the action of wind, waves, rain, or thermal effects. It can also be generated by shear beneath the surface, for example from internal waves on a pycnocline, or the bottom boundary layer in open channel flows or barotropically

and baroclinically driven flows along the coast, in estuaries, or in lakes. We consider the case of turbulence generated beneath the free surface because it allows us to create well-conditioned, nearly homogeneous turbulence and isolate its effect on gas transfer. Understanding gained from this system can help inform companion studies of how eddies from other sources (even non-turbulent ones) effect transfer.

1.2 Previous Work

The major research topics relevant to this work are listed below, and will be discussed in the following subsections. This review is limited to studies of interfaces not subject to mean shear. This excludes studies of wind-generated waves, an important and related topic which is discussed in an excellent review by Banerjee and McIntyre (2004).

Terminology used here is as follows. U,V, and W are the instantaneous velocities, and < > denotes time averaging. Instantaneous fluctuating velocities are u' = U-<U>. RMS turbulent velocities are $u_{rms} = \langle u'^2 \rangle^{1/2}$. Z is defined as the surface-normal direction, with positive upwards, and W the surface-normal velocity. X and Y follow the right-hand rule. Results from studies in which Y was the surface-normal direction are translated into the Z-normal terminology. U and V are referred to as the tangential velocities. η is the free surface elevation *and* the Kolmogorov length scale. The meaning should be evident from the context. η' is the fluctuating free surface height, and $\eta_{rms} = \langle \eta'^2 \rangle^{1/2}$. ε is the viscous dissipation rate. The Schmidt number $Sc = \nu/D$, where ν is kinematic viscosity and D is the molecular diffusivity of a scalar. Prandtl number Pr is the same as the Schmidt number, but used when the scalar of interest is heat.

1.3 The effect of a no-slip boundary (i.e. wall) on turbulence with no mean shear at the wall

Boundary conditions for this case are U = V = W = u' = v' = w' = 0, du'/dx=0, dv'/dy=0, dw'/dz = 0. The surface acts to redistribute energy from surface-normal (w_{rms}) to surface-tangent (u_{rms},v_{rms}) motions. Hunt and Graham (1978) explore this effect analytically by considering a flat plate suddenly appearing in a turbulent flow and moving at the flow's mean velocity. Rapid Distortion Theory is applied and the authors show that decay of w_{rms} towards the boundary can be described by considering the boundary as a "source" of *negative* rms velocity. Hence this is sometimes referred to as the 'source theory' of Hunt and Graham; it is also called the 'linear theory' and the 'blocking theory'. This work includes a prediction of the wall's effect on velocity power spectra as well as fluctuating velocity profiles.

These predictions are updated in Hunt (1984) for the case of turbulent flows with zero mean flow, such as turbulent convective flows or grid-stirred tanks. This takes the form of a nonlinear correction to the linear theory. It incorporates the effect of distorted large eddies on the vorticity of small eddies, and results in a further increase of velocity fluctuations tangent to the free surface. Both the linear (1978) theory and the 1984 nonlinear correction are derived for developing flows, valid for times less than one eddy turnover time from when the boundary suddenly appears. However, the authors hypothesize that their results are valid for statistically steady flows as well. This hypothesis is supported in the case of high Reynolds number flows by the analytical work of Magnaudet (2003). In this work, Magnaudet also gives strong evidence for replacing Hunt's 1984 nonlinear correction with a different nonlinear correction that shows a smaller increase (with respect to the linear theory) in tangential rms velocities.

Experiments and LES studies support that validity of Hunt and Graham's 1978 theory (and subsequent corrections) for statistically steady flows. The LES of Calmet and Magnaudet (2003) for the shear-free free surface of an open-channel flow shows excellent agreement. The ADV measurements in a grid-stirred tank by McKenna and McGillis (2000) agree with velocity profiles in a qualitative sense. A major piece of supporting evidence is the hotwire measurements of Brumley and Jirka (1987) in a grid-stirred tank. While most experiments validate only Hunt and Graham's predictions of rms velocity vertical profiles, Brumley and Jirka also show good comparison between the predicted power spectra, which show reduced amplitude at low-wavenumbers near the free surface. Law, Khoo, and Chew's (1999) PIV study of round jet turbulence impacting a free-shear interface uses advanced free-surface tracking to show that agreement with Hunt and Graham's (1978) predictions improve when fluctuating vertical velocities are corrected with respect to the moving free surface ($w'_{improved} = w' - d\eta'/dt$).

It is interesting that these agreements exist despite the fact that experiments are beneath shear-free free surfaces, while the theory was developed for a shear-free no-slip boundary. Perot and Moin (1995) find that the transfer of momentum from surface-normal to surface-tangent motions is much smaller beneath a free surface than beneath a solid wall. This makes it even more surprising that Hunt and Graham's predictions hold so well for free surface flows.

1.4 The effect of a free surface on bottom-generated turbulence with no mean shear at the surface

Unlike a no-slip wall, a free surface can support nonzero values of u' and v'. In an Eulerian sense a deformable free surface can show w' variations as well, which are equivalent to free surface elevation changes η'. Referenced to the free surface

location, however, w' must be zero. Surface divergence can be nonzero at a free surface, and continuity gives $du'/dx + dv'/dy = - dw'/dz$. As the boundary condition is shear-free, the free surface cannot support a mean shear, thus $du/dz = 0$ and $dv/dz = 0$ at the surface. Similar to the no-slip boundary discussed above, fluctuating velocities display intercomponent energy transfer near a free surface, but this effect is smaller than that observed at a no-slip boundary (Perot and Moin 1995).

DNS by Perot and Moin (1995), Walker *et* al (1996), and Nagaosa (1999) all study channel flow with a free-shear free surface. They are at lower Re than the analytics discussed above, as well as the LES and experiments used to justify the analytical results. All three works agree on a direct physical explanation of the energy transfer from surface-normal to surface-tangent motions. That is, there is an imbalance between the effects of upwelling and downwelling events (discussed in section 1.6) on the normal component of the pressure-strain correlation, Π_{33} . This quantity is defined as $\Pi_{ij} = \langle p' S_{ij}' \rangle$ where p' is the fluctuating pressure value and S_{ij}' is the instantaneous fluctuating symmetric velocity gradient tensor. Upwellings are negative contributions to Π_{33}, while downwellings have the opposite effect (Magnaudet 2003). Negative values of Π_{33} result in the transfer of momentum to surface-tangent motions. Thus if the turbulent structures near the free surface are such that downwellings' contributions to Π_{33} are less than those of upwellings, there will be a net transfer of energy from surface-normal to surface-tangent motions. The three papers disagree on the source of the asymmetry between upwelling and downwelling's contribution to Π_{33}, as discussed in Magnaudet (2003).

This focus on the pressure-strain correlation mechanism is effectively a paradigm shift in how we study the effect of a free surface. It reduces the emphasis on bulk turbulent quantities and instead focused on the "zoology" of coherent surface structures. It is important to note however that coherent structures' properties depend

on the source of the subsurface turbulence (discussed in section 1.6). Thus there can be very different near-surface behavior, and thus mass transfer, between channel flows, grid turbulence (used herein to describe turbulence from mean flow past a grid), and zero-mean flow turbulence (from a grid-stirred tank or our random jet array) even with the same turbulent Reynolds number ($Re_T = u_{rms}L/\nu$).

The difference between no-slip and free surface boundaries is significant for scalar transport processes. Jahne and Haussecker (1998) review how the dimensionless transfer resistance r = u*/K, where u* is the friction velocity and K is the mass transfer velocity, scales as $Sc^{2/3}$ at a solid wall and as $Sc^{1/2}$ at a free-shear interface. At Sc=600 (CO_2 gas at 20˚ C) and holding u* constant, changing from a no-slip wall to a free surface is equivalent to roughly a factor of 3 increase in the gas transfer velocity K. McCready and Hanrattty's (1984) analytical work confirms this.

A second important difference between free surface and no-slip interfaces is a change in the size range of motions relevant to scalar transfer. Campbell and Hanratty's (1983) analytic work for high Sc find that low frequency fluctuations dominate at solid walls; further work by McCready and Hanratty (1984) show that at free surface interfaces higher frequency motions are not damped as much, and thus become important for gas transfer.

1.5 The effect of approximating the free surface as stationary, when it is deformable

Free surface deformations are unavoidable in experiments, though it is possible to use surfactant layers to damp such motions. In numerical simulations, however, it is easy (and time-saving) to neglect deformations. Thus the effects of free surface deformations is discussed mostly in the context of numerical work. Whether these effects are negligible or not appears to remain an open question at this time.

Pan and Banerjee (1995), analyzing the DNS of Komori et al (1993), claim that allowing small amplitude free surface variations do not give significantly different results compared to a nondeformable surface. Nagaosa (1999) makes a similar claim, stating that Borue *et al* (1995) and Tsai (1996, 1998) see no noticeable effect of free surface deformations on turbulence statistics. Nagaosa explains that this is due to the low Re of the flows. Despite these claims, many other researchers assert that free surface fluctuations do have a noticeable effect on near-surface flow.

The work by Tsai (1998) that was discussed by Nagaosa (1999) reports nonzero correlations between coherent structures and free surface height. His observations make good physical sense in the context of coherent structures described in section 1.6. He reports free surface depressions at the center of spiral eddies (such dimples are easy to see in a river). He also reports surface curvature correlated with subsurface regions of surface-tangent vorticity. Whether these or other free surface deformations are essential for describing the physics of mass transfer across the free surface remains to be seen.

The DNS of Lakehal, Fulgosi, Yadigaroglu and Banerjee (2003) allowed small surface deformations of a free shear interface. While their study focused on the gas side of a sheared interface, their comparison of results between deformable and nondeformable surfaces are worth noting. They find that interfacial deformations reduce the magnitude of the turbulent fluctuations near the interface and thus give a reduced dissipation rate there.

Banerjee and McIntyre (2004) note that a deformable interface will reduce the amount of surface divergence. Because gas transfer is hypothesized to scale as the square root of surface divergence (see section 1.7) this result suggests that allowing a surface to deform will reduce the gas transfer rate. Thus simulations of mass transfer with a nondeformable free surface may overestimate the transfer rate.

1.6 Coherent surface structures

The three coherent surface structures (in the absence of mean shear at the interface) are upwellings, downwellings, and spiral eddies. Upwellings, also called updraughts or splats, are characterized by increased vertical fluctuating velocity ($w' > 0$), free surface height ($\eta' > 0$), and pressure ($p' > 0$). Upwellings' cross sections on the surface vary from roughly circular to very elongated, depending on the shape of the subsurface structure causing it. Downwellings, also called downdraughts, anti-splats, or surface patches, show $w' < 0$, and likely $\eta' < 0$ and $p' < 0$ as well. They are companion events to the upwellings, because continuity requires a downward flow to compensate for the upward flow. Spiral eddies (also called surface-attached vortices) are long-lived 'whirlpools' on the surface with strong vertical vorticity.

1.6.a Genesis of surface structures in channel flow

In channel flows, all three structures are attributed to the interaction between the free surface and rising subsurface 'hairpin vortices'. These are a pair of counterrotating vortex tube 'legs' oriented in the streamwise direction and joined at a 'head', where the curvature is very sharp, as in a hairpin. There is strong evidence that they form around streamwise streaks of low speed fluid ejected from the bottom boundary layer. Rashidi (1997) shows that it is common for only half of a hairpin vortex to form, having one leg and resembling a hockey stick. Interestingly, Tsai (1996 and 1998) observes hairpin vortices created far from a boundary layer, developing from an initially random vorticity field with mean shear.

As they approach the surface, different behaviors are reported for hairpin eddies' creation of surface structures. Nagaosa and Handler (2003) report that they become ring-like vortices with upwelling flow in their centers, while Rashidi (1997) says that the 'head' ejects a series of upward bursts of vortical momentum. Nagaosa

(1999) hypothesizes that legs could align parallel to the surface, with each leg sweeping fluid upward along one of its sides and downwards on the other side, but such features are not observed in his channel flow DNS. Pan and Banerjee also report no surface-parallel streamwise vortex tubes near the free surface, noting that this may be the influence of the free-surface constraint that surface-tangent vorticity must go to zero. They say this causes surface-parallel vorticity to reorient to the surface-normal direction, where it can create or connect with spiral eddies.

Spiral eddies have been attributed to the reorientation of the 'legs' of hairpin vortices and subsequent attachment to the surface (Tsai 1998, Nagaosa 1999). Alternatively, Pan and Banerjee (1993) report that vortices are formed by the surface shear either at the edge of upwellings or between upwellings and downwellings. They describe how this formation is related to streamwise vortex tubes, but whether these are the 'legs' of hairpin vortices is unclear. Tamburrino and Gulliver (2002) also observe the creation of vortices at the edge of upwellings.

We note that our flow will not have hairpin vortices, thus coherent surface structures will be formed by other phenomena, such as rising canonical turbulent eddies. The mechanics of surface structure formation by these eddies will likely be related to at least some proposed mechanisms of their formation by hairpin vortices.

1.6.b Effect on mass transfer

On average, Upwellings bring bulk fluid towards the surface. Since this bulk fluid has a lower scalar concentration than in the near-surface concentration boundary layer (CBL), upwellings also have a signature of $c' < 0$, giving a negative mass flux $w'c'$, which indicates scalar transfer from the interface into the bulk. As upwellings bring low-concentration bulk fluid towards the free surface, they thin the CBL, indirectly increasing the mass transfer rate. By steepening the near-surface

concentration gradient, they increase the rate of molecular diffusion. This is the basis for the surface renewal models discussed in section 1.7.

Downwellings can be found at convergence zones between two adjacent upwellings, or at the edge of a single upwelling. Downwellings contribute to scalar transfer directly by transporting the high-concentration fluid near the surface into the bulk, where it is rapidly mixed due to higher turbulent levels there. Jahne and Haussecker (1998) cite results from Jahne (1993) showing that parts of the CBL are swept into the bulk. Herlina and Jirka (2004) also observe such behavior using LIF in a grid-stirred tank: "…portions of the surface layer with a higher oxygen concentration was peeled off by a turbulent structure and then transported into the bulk region." Neither explicitly mention this as a process driven by downwelling. On the contrary, Herlina and Jirka interpret this effect as evidence for the upwelling-based surface renewal models.

Spiral eddies are long-lived and show a slightly downward mean velocity (Kumar *et al.* 1998). Thus they could hypothetically act as a pump for moving the CBL fluid into the bulk. Contrary to this hypothesis Nagaosa reports that these have negligible effect on scalar transport, but this analysis uses the value of $(dc'/dz)_{surf}$ as an indicator of transfer, rather than the more direct w'c', which was available in their dataset. Analysis by Kumar *et al* (1998) based on surface divergence theory (described in section 1.7) and experimental measurements of dw'/dz in channel flow suggest that mass transfer by spiral eddies may have effects comparable to those of upwellings, causing 20% of total mass transfer while upwellings cause 50%. This being a preliminary measurement, the remaining 30% is not discussed, nor is the source of their total mass flux value. Tamburrino and Gulliver (2002) report that the strongest values of surface divergence, and thus mass transfer (see section 1.7.b) are located above flow features closely resembling spiral eddies.

In this work we observe that downwellings are more concentrated (larger vertical velocity over a smaller area) than upwellings, while Perot and Moin (1995) suggest the opposite is true, claiming that downwellings are diffuse compared to upwelling motions. The resolution to this conflict is likely in the fact that the properties of free surface structures depend sensitively on the properties of bulk turbulence. When hairpin vortices are present, as in channel flow, there is little reason to expect the same free surface statistics as in grid turbulence or zero-mean-flow turbulence. To date, there have been no studies, either experimental or numerical, of coherent surface structures above zero-mean-flow turbulence. A census of the type, number and size of coherent structures in our flow will be a useful result, as our system is closer to canonical turbulence than the open channel flows in which free surface structures have been explored.

1.7 Existing models' and parameterizations' attempts at describing such phenomena via easily measurable properties

Surface renewal (SR) models describe mass transfer in terms of the upwellings, which they term surface renewal eddies. Dankwert's work extending Higbie's model gave $K \sim (D\tau)^{1/2}$ where τ is a surface renewal frequency. The two leading SR models, by Lamont and Scott (1970) and Fortescue and Pearson (1967), both parameterize τ in terms of properties of the turbulent flow in the bulk.

Surface penetration (SP) models are a more detailed form of SR models, in which upwellings do not completely renew the surface but rather follow a distribution of approach distances. Asher *et al* (2004) shows that SP models reduce to SR models when the scalar boundary layer is thick enough to include this entire range of approach distances. This is the case, for example, in heat transfer, but not for the thin CBL of interest in CO_2 transfer.

Surface divergence (SD) models describe mass transfer in terms of regions of divergence and convergence on the free surface. The sources of such regions include the same upwellings considered in SR models, but also include downwellings and possibly spiral eddies. Two versions of SD models are derived by Hanratty (1990) and Banerjee (1990). In a strikingly similar form to the SR models, both of these models show that for high Sc number gas transfer under a free-shear interface $K \sim (D\gamma_{rms})^{1/2}$. Here, γ is the surface divergence $\gamma = (du'/dx + dv'/dy)_{surf} = -(dw'/dz)_{surf}$ and $\gamma_{rms} = <\gamma^2>^{1/2}$. Several methods of computing γ, γ_{rms}, and related quantities for use in this and similar relations are discussed below.

Turbulent diffusivity (TD) models are based on the idea of turbulent diffusivity, an idea which has proved useful despite serious flaws (Pope 2000 ch 4.4, 10.1). Taylor expansions near the interface show that the turbulent diffusivity is an increasing function of distance from the surface, $D_t \sim z^2$ for no-slip interfaces and $\sim z^3$ for free surfaces. Henstock and Hanratty (1979) show that in limiting cases these models have the same results as SR models (as cited in Banerjee 1990).

1.7.a Surface Renewal (SR) models and the size of motions relevant to scalar transfer

The size and type of motions responsible for the mass transfer remains an open question, and an often-discussed one for SR models. Fortescue and Pearson's SR model (1967) consider the largest eddies, with diameter being equal to the bulk integral length scale, to dominate gas transfer. This results in setting $\tau = u_{rms}/L$ (recall $K \sim (D\tau)^{1/2}$ where τ is a surface renewal frequency). Lamont and Scott (1970), and the preceding work by Banerjee, Rhodes, and Scott (1968), focus instead on the smallest eddies. Their analysis reveals however, that "…the mass transfer is not due to any narrow range of scales of motion, but is due to scales which extend from the smallest

viscous motions well into the inertial motions, with only a minor preference for the smaller scales." By integrating the effects of many size eddies, using a model spectrum, they determine $\tau = (\varepsilon/\nu)^{1/2}$. We emphasize that this is *not* a small eddy result, as is often written, but rather takes into account a wide range of eddies from size 4.27η to roughly 80η, thereby including a portion of the dissipation and inertial ranges.

Recent DNS work shows that the size of motions that dominate gas transfer depend on both the molecular diffusivity of the scalar and the type of boundary across which gas transfer occurs. Campbell and Hanratty (1983) found that low frequency fluctuations dominate at solid walls for high Sc; further work by McCready and Hanratty (1984) show that at free shear interfaces higher frequency motions are not damped as much, and thus are important for gas transfer. Na and Hanratty (2000) show a large flat region in the heat flux spectrum below a sheared no-slip interface, indicating that motions of many sizes contribute equally to the gas transfer for this case. Nagaosa and Handler (2003) report that for Pr =1 the mass transfer by small eddies is negligible compared to that accomplished by integral-length scale motions, specifically those of the coherent structures discussed above.

The question of which size motions dominate gas transfer is also present in the context of SD models, for which Gulliver and Tamburrino (2002) find that large-scale motions dominate while McCready *et al*. (1986) find that motions covering a wide range of scales all contribute equally.

1.7.b Surface Divergence (SD) Models

SD models currently use a variety of measures for the surface divergence. Interestingly, all are seen to give good agreement with experiments, even when the surface flow conditions are varied widely.

McCready *et al*. (1986) determine that for a shear-free solid wall, only the lowest frequencies matter, thus the relevant surface-divergence value is the lowest frequency component of the fluctuating surface divergence, which can be extrapolated from the surface divergence spectrum. For a shear-free free surface, they note that the entire range of motions matters, thus they parameterize K in terms of a model spectrum, whose amplitude is proportional to γ_{rms} and whose shape contributes to the constant of proportionality. The resulting parameterization is $K \sim (D\gamma_{rms})^{1/2}$.

Banerjee (1990) calculates γ_{rms} in terms of bulk turbulent quantities by integrating the surface divergence spectra obtained by Brumley and Jirka in an extension of the results of Hunt and Graham. This gives a parameterization of K as a function of Sc and Re_T.

Turney *et al* (2004) measure the free surface velocity field directly with PIV and calculate γ_{rms} directly from this. Their results show a linear relationship between K and $(D\gamma_{rms})^{1/2}$, with $R^2 = 0.95$. We observe that the largest deviations from linear behavior occur at their lowest values of γ_{rms}. Unlike other studies discussed here, this work was performed in a linear wind-wave tunnel, with surface turbulence caused by mean shear at the free surface.

McKenna and McGillis measure the surface divergence field directly with PIV and compute two values depending on how they collected their data: a_1 = spatially averaged surface divergence magnitude, and a_2 = integral of surface divergence temporal spectrum (30 hz sample rate) at a single point. They consider these measures as describing the same physical quantity, thus $a = a_1 = a_2$, though they do not test this

equivalence. Plotting bulk gas transfer rate K vs $a^{1/2}$, McKenna and McGillis find good collapse onto a single curve. This is remarkable because their data is from experiments including a variety of phenomena including one or more of the following: subsurface turbulence, surface waves, and surfactant layers. This result is exciting and the physical reasoning behind it makes good sense, but the collapse is not perfect, the scatter being roughly 50% variability in K for a given value of a.

Law and Khoo (2002) find that $\gamma = (dw'/dz)_{surf}$ can be evaluated from subsurface measurements, since within a small distance of the free surface (~3 mm in their work) w' is linear with z. This linear region is predicted by McCready *et al.* (1986) by use of a Taylor expansion of w' at the surface. To observe this linear region, both w' and z must be corrected with respect to the fluctuating free surface height and velocity. The slope over this linear region is labeled β, and is identical to γ assuming the linear relation holds all the way to the free surface. While their data allow for calculation of instantaneous β values, from which $\gamma_{rms} = <\beta^2>^{1/2}$ can be calculated, Law and Khoo (2002) parameterize gas transfer based on a different value. They work with a quantity $\beta_2 \equiv dw_{rms}/dz$ (they call this quantity β_{rms}, but I have changed the name for clarity of notation). Their choice of this quantity is puzzling – since there is no equivalent to the continuity relationship for rms velocities, β_2 is not directly related to the surface divergence. Nonetheless their results show an excellent collapse. Gas transfer velocity scales linearly with $(D\beta_2)^{1/2}$ with an R^2 value of 0.98. These data were taken for flows with several different kinematic viscosities in which turbulence was generated by a single submerged jet pointing at the surface, and for flow in a wind-wave tank. The wind-wave data differs slightly from the linear behavior, but this effect is minimal since the R^2 value of 0.98 includes this data.

It is an open question whether SD models includes the effects of spiral eddies which as indicated above may have a strong effect on mass transfer. Measurements by

Gulliver and Tamburrino (2002) show that the largest β values are found at highly divergent eddies at the edge of upwellings. We recall that Pan and Banerjee (1993) observe the formation of spiral eddies at the edge of upwellings as well. In a contrasting view, Handler *et al* (2003) state that spiral eddies exhibit very small divergence, inducing surface flow along nearly circular streamlines. It is possible that the divergent eddies at the edge of upwellings may be an early stage of the low-divergence spiral eddies, or a different class of surface structure entirely.

1.7.c Downwellings in the SR and SD models

In addition to the support from the experiments listed above, the SD model is appealing because it includes the effects of downwellings. Surface convergence above a downwelling will enter as a positive contribution to the rms surface divergence, thus it acts to increase the mean gas transfer rate. As discussed in section 1.6.b, these regions may be a central component of gas transfer. Inclusion of these may be one reason for SD model's apparent success in parameterizing gas transfer.

When used under the conditions for which they were developed, the SR models perform roughly as well as the SD models. They can do so despite not explicitly including the effect of downwellings for a simple reason – downwellings and upwellings are intricately related via continuity. A model parameterized based on number, size, or energy of upwellings contains implicit assumptions about the statistics of downwellings. Thus a surface renewal model can still describe the effects of downwellings. This was well understood by Fortescue and Pearson, who note the effect of downwellings at the edge of their modeled surface renewal eddy: "The absorbed gas is carried into the bulk of the fluid largely by the layers of 'surface' fluid that plunge downwards near the edge of the eddy."

1.8 How these effects vary with the scalar's molecular diffusivity

Transfer of CO_2 across an interface likely shares some characteristics with the transfer of heat and momentum, but these analogies are limited by the fact that CO_2 is much less diffusive than than these other quantities. Using these analogies correctly requires the consideration of how scalar transfer changes with a scalar's molecular diffusivity.

DNS of the air-side dynamics of heat transfer by Na and Hanratty (2000) shows that large wavenumber motions contribute less to transfer as Pr rises from 1 to 10. In a similar study, Lakehal *et al.* (2003) consider the budgets for turbulent heat transfer, showing that the production and dissipation both increase with Pr from 1 to 10. As Sc (or Pr) increases, control of the transfer process shifts from the air side to the water side (Jahne and Haussecker 1998). In this water-side-controlled regime, experiment and theory show that the bulk scalar transfer rate $K \sim Sc^{-1/2}$.

Once transfer processes are dominated by water-side motions, further increase in Sc causes the CBL to become thinner. Once the entire CBL is thin enough to fit within the viscous momentum boundary layer, it is "shielded" from the effects of turbulence. As the CBL "retreats" into the momentum boundary layer, we expect that the effects of upwellings, downwellings, and spiral eddies on the CBL will change. Thus the relative importance of these mechanisms may change with Sc.

Finally, Jahne and Haussecker (1998) remind us of temperature's strong effect on D, and thus Sc. They point out that for many scalars, Sc typically changes by roughly a factor of 5 as temperature rises from 0 to 35 C.

1.9. The effect of a surfactant layer on the turbulence-boundary interaction and mass transfer mechanisms

The presence of a surfactant layer directly reduces the rate of molecular diffusion of scalars across the interface. Furthermore, it changes the interactions between the interface and subsurface turbulence that give rise to the turbulent scalar transfer enhancement. Tsai (1996) suggests that the latter effect dominates. Surfactants exhibit an elastic force that acts to counteract the effects of surface divergence, thus modifying the near-surface flow dynamics. These modifications are considered below, first in terms of mean quantities and then in terms of the dynamics of coherent structures.

Tsai (1996) reports that while under clean interfaces w_{rms} decreases and the momentum is tramsferred into u_{rms} and v_{rms}, under a contaminated interface all three components decrease monotonically. This effect is confirmed by the DNS of Handler *et al* (2003). However, the surfactant is not simply creating a wall effect, seen in the fact that u_{rms} and v_{rms} remain nonzero at the interface, since the surface still supports shear. Handler *et al* (2003) predict an increase in the dissipation rate for surfactant-covered interfaces.

Bernal *et al* (2001) show that both vortex rings and vortex pairs, when interacting with a free surface, generate secondary vorticity that causes them to rebound from the free surface. Surfactants have a significant effect on this process – under cleaner surfaces the secondary vorticity evolves more slowly, thereby reducing the rebound effect and allowing the primary vortices to remain near the free surface longer. While at the free surface, the primary vortices spread out in the tangential directions, with upwelling and downwelling regions along their edges. Thus the lower surfactant concentrations lead to longer residence times at the surface, during which the vortex will effect a larger area of the free surface, and thus produce more scalar

transport. Tsai (1996) shows similar results in which the presence of surfactants causes secondary vortices to form in response to upwellings, reducing their approach distance and residence time at the surface. Thus we expect surfactants to reduce the effect of upwellings on gas transfer. Since upwellings thin the concentration boundary layer, surfactant layers should have thicker CBLs. This effect is reported by Handler *et al* (2003).

Tsai (1996) indicates a decrease in the number or strength of surface attached vortices present under contaminated conditions. He reports that under a clean free surface, the dominant component of vorticity is vertical, but the introduction of a surfactant decreases the enstrophy of this vorticity component is reduced by a factor of 2 while the other two components increase. Handler *et al* (2003) observe a similar behavior for the vorticity; $\omega_3 = dV/dX - dU/dY$ decreases by 20% for the highest surfactant concentration studied, corresponding to an enstrophy decrease of about 1/3. The authors point out, however, that this decrease is minor compared to the increase in surface tangent vorticity components. They explain that the surface-normal vortical motions (dominated by spiral eddies) have very small divergence, and thus compress the surfactant only slightly, thereby contributing very little elastic effect to these motions.

The increase in surface-tangent vorticity is explained by the surfactant layer's ability to support an instantaneous surface shear. This has a second interesting effect, hypothesized by Handler *et al* (2003), in which fluctuating shear at the surface can produce coherent structures similar to those seen in a no-slip boundary layer, namely low speed 'streaks' injected into the bulk. Thus a fourth coherent structure is possible for the surfactant case, and the streak joins the upwellings, downwellings, and spiral eddies. Since an injection from the surface would directly transfer mass from the CBL into the bulk (like downwellings do) this would constitute a surfactant-induced

increase in mass transfer, though the effect is clearly outweighed by surfactants' other transfer-reducing effects.

No work has commented on the effect of surfactants on downwellings or downwelling-enhanced mass flux. We can reason that since surfactants make upwellings weaker, shorter, smaller, or less frequent at the free surface, then by continuity the downwelling momentum must be reduced there as well. However, the mechanism of downwelling-enhanced scalar flux is different from upwelling-induced scalar flux. Thus it is not certain that weakening downwellings will decrease the downwelling-induced scalar flux in the same ratio as weakening upwellings decreases the upwelling-induced flux.

It is evident from this discussion that surfactants will likely have a different damping effect on upwellings, downwellings, and surface attached vortices. Thus the understanding of each of these mechanisms for gas transfer will be important in understanding how gas transfer rate changes with surfactants.

McKenna and McGillis (2000) show that the surfactant layer can decrease gas transfer velocity by a factor of 2 to10, the factor increasing with the strength of subsurface turbulence. Asher and Pankow (1986) show a similar effect.

Only a small fraction of the ocean surface is covered by high-concentration surfactant films (GESAMP 1995). However, even low concentrations of surfactants can have a significant effect on gas transfer, and efforts are currently underway to improve our understanding of the contribution of a variety of surfactants on the ocean surface.

It is important to note that all surfactants do not have the same effect – Bock and Frew (1993) report that the elastic properties of surface films are highly variable. Depending on their source and location, surfactants' damping of capillary waves occurs in different frequency ranges (and this damping effect is not always unimodally distributed across frequencies).

CHAPTER 2

EXPERIMENTAL TECHNIQUE

2.1 Experimental Setup in brief

We perform a series of laboratory experiments in which pure CO_2 gas fills the headspace above a tank of distilled water with a low concentration of dissolved CO_2. Turbulence is generated in the headspace by a single round jet supplying the CO_2 gas (Jet Re = 100,000), and at the bottom of the tank by an array of synthetic jets. These bottom jets are zero net mass flux jets, introducing momentum and strong shear at the bottom of the tank in a random manner. The momentum and shear evolve into nearly isotropic turbulence some distance above the jet array. This turbulence then transports itself upward (not via mean upward flow, but by the turbulent transport of turbulent energy) towards the free surface. This turbulence generation system was designed to minimize mean flows, which can have a large effect on gas transfer when they steadily draw the surface layer into the bulk.

We take simultaneous measurements of the 2D velocity and concentration fields in a plane orthogonal to and intersecting the free surface (see Figure 1). These are done in a non-invasive manner via high-resolution digital imaging of an area illuminated with a planar laser light sheet. Velocity fields are determined from particle image velocimetry, PIV, in which we correlate the position of effectively passive (Stokes number < 0.05) tracer particles in successive images. Concentration fields are from laser induced fluorescence, LIF, in which a fluorescent dye, well-mixed in the tank, fluoresces in proportion to the local CO_2 concentration (concentration denoted herein by []). This fluorescence decreases as $[CO_2]$ increases, and we calibrate this relationship by measuring the bulk pH with two electrodes.

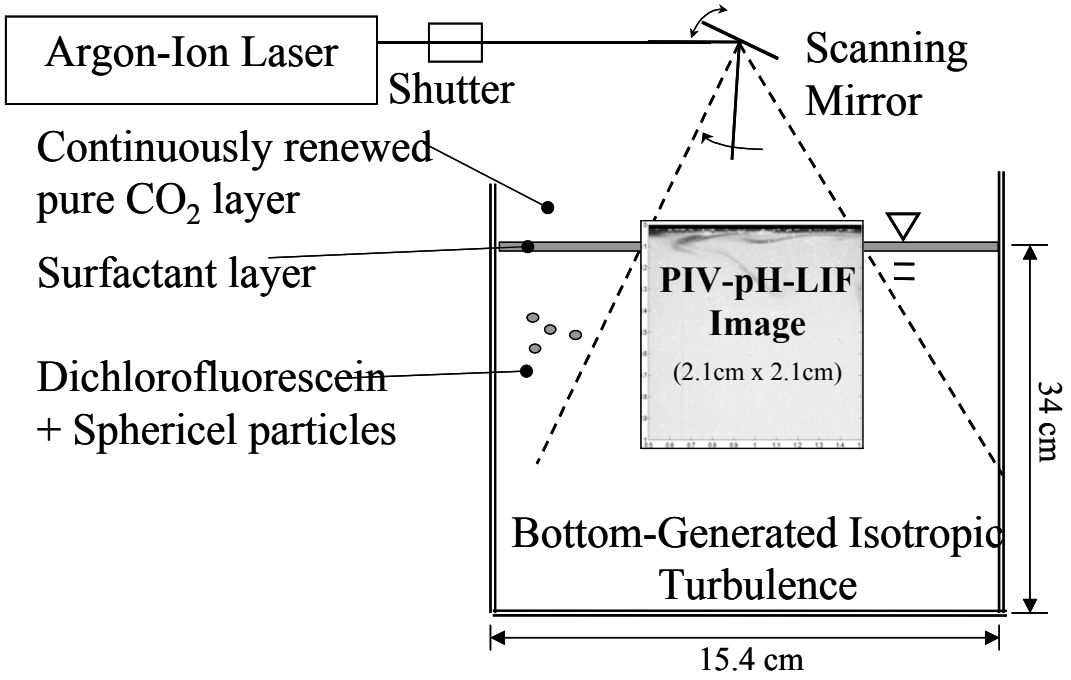

Figure 1. Experimental setup. We attempt to minimize the thickness of the surfactant layer, but without extreme effort some will remain.

For the data reported here, our image area is 2.1 cm by 2.1 cm, spatial resolution is 25.4 micron for LIF and 813 microns for PIV. The tank is 15.4 cm x 15.4 cm with 34 cm water depth. The turbulent Reynolds number is ~120, and the Taylor microscale Reynolds number R_λ is ~40. The Kolmogorov length scale is ~100 microns. Data is collected at 1.25 hz for 6 minutes, to allow for robust ensemble averaging of temporally independent data samples. Details of the experimental setup and imaging techniques follow.

2.2 Water Chemistry

Distilled water (0.25 MΩ) is allowed to equilibrate with the atmosphere, then stripped of CO_2 by bubbling with He through a diffuser stone. NaCl is added to 0.01 molar, which will provide a known and effectively constant ionic strength, which will

be of use when inferring bulk [CO_2] from pH electrode readings. The fluorescent dye, 2',7' dichlorofluorescein (Acros Organics, distributed by Fisher Scientific), is added to 0.04 micromolar and well-mixed throughout the tank to allow the LIF technique. Hollow glass spheres (Sphericel, Potters Industries) are placed in solution and allowed to sit for >2 hours, after which only those which are neutrally buoyant are siphoned off and added to the tank at a concentration so that particles occupy roughly 1% of the pixels in each image (~100 ppm). This also serves to rinse manufacturing-related chemicals from the particles, which McKenna and McGillis (2000) show can be a significant source of surfactants.

Any surface contamination, especially a surfactant layer, can radically change the gas transfer physics. To keep the surface as clean as possible, we skim the water surface immediately before the experiment. This is done by constantly adding water to the tank bottom while an overflow drain at the free surface level allows the surface layer, and any contaminant on it, to leave the tank. As the free surface cleanliness increases during skimming, digital images show a decreasing amount of reflection by the free surface, and He bubbles spend less time on the underside of the free surface before bursting. The overflow drain is a push-lock fitting permanently mounted in the side of the tank at the desired free surface height. The geometry of this fitting in the area where the water spills over has the form of a broad-crested weir; in future experiments we will switch to a sharp-crested skim drain with an adjustable height. Over time, surfactants leach from the submerged equipment and materials, thus we keep our experiment short (6 minutes) in the hope of maintaining a constant surfactant thickness.

2.3 Turbulence Generation

The experiment discussed here was performed in a prototype of a tank which was designed specifically for this research. The prototype is 15.4 cm x 15.4 cm x 40 cm deep, while the full-size facility is 80 cm x 80 cm x 80 cm. Both make use of a novel turbulence generation mechanism.

The grid stirred tank (GST) is the standard facility for studying turbulence in the absence of advection (DeSilva and Fernando 1994, Brumley and Jirka 1987). All GSTs, however, are susceptible to secondary flows from several sources (Fernando and DeSilva 1993). Due to its highly mechanical nature, a GST exhibits irregularities in the drive motor, multiple drive shafts which are difficult to align (or grid wobble if there is only one shaft), and departure from pure grid geometry where the drive shaft(s) meet the grid. The GST boundary conditions suffer due to a finite gap between grid edges and the wall. Furthermore, many designs have surface-piercing elements that can impede measurements at the free surface and generate surface capillary waves. The deterministic nature of the grid motion can permit secondary flows, once established, to persist in a dynamic equilibrium.

Researchers working over the past 30 years with several different facilities typically report that secondary flows are present but negligible. We consider the ratio of mean velocity to rms turbulent velocity $R = \langle U \rangle / U'$. Reported and inferred values from a variety of GST experiments show R is typically about 0.25 with a best case value of R in a single coordinate direction (Variano *et al.* 2005). In the worst case R can exceed 1. Whether it is fair to neglect secondary flows of this magnitude depends on the purpose of each experiment; in our case the removal of advective transport will greatly increase the accuracy of our measurement of turbulent scalar transfer.

Our new means of generating turbulence beneath an undisturbed free surface was inspired by the extremely successful active wind tunnel grid of Mydlarski and Warhaft (1996) as well as the synthetic jet-generated turbulence facility of Hwang and Eaton (2004). It is an array of vertically oriented synthetic jets, each switching on and off randomly, generating turbulence from below with minimal disruption of the free surface. Synthetic jets are those with zero net mass flux, integrated over either space or time. This can be achieved with an incurrent and excurrent port coupled via a pump or a single port that oscillates in time between incurrent and excurrent flows. We use the former method, with 16 jets in our prototype tank and 64 in our full-size facility.

As distance from the orifice plane increases, the synthetic jets merge as do the grid wakes in a GST, and initial anisotropy from the jets is erased by the turbulent stirring (Villermaux and Hopfinger 1994). Random forcing should prevent most sources of secondary flow, and greatly reduce the opportunity for secondary flow to persist if established. By adjusting the parameters of the random forcing, we can select a range of frequencies at which to drive the tank, essentially choosing the integral length scale and low wavenumber region of the power spectrum.

Results from the prototype tank (in which we performed the gas transfer experiments discussed here) show a mean value of $\langle U \rangle / U' = 0.16$. The same quantity for several different GSTs (collected from the literature) is 0.34 (Variano *et al.* 2005). Similarly, the median values are 0.09 and 0.25, for our random jet array and the GSTs respectively. Bootstrap analysis shows that this superior performance of the random jet array is significant at the 95% confidence level (Efron and Tibshirani 1993). This reduced mean flow may result in a smaller gas transfer rate in this tank compared to GSTs.

2.4 Imaging & Illuminaton

Data discussed below shows that 2 cm is an ideal image area size. It allows us to resolve the concentration and momentum boundary layers near the surface, and includes data far enough from the surface (~4 integral lengthscales) to be considered representative of bulk fluid properties. Comparisons between bulk fluid and surface fluid will be important for the analysis which follows.

Our digital CCD camera is a Dalsa SMD1M30, 12 bits per pixel, 1024 x 1024 pixels, full-frame transfer camera with 30 Hz maximum frame rate and 2.17 ms minimum time between exposures. A 105 mm Nikkor telephoto lens allows us to image the desired area of 2cm by 2cm located ~30 cm from the camera. We use the minimum f-stop of 2.8 to increase the amount of light exposing the CCD chip, increase linearity, and recuce the effects of out-of-plane scattered light. Images are written directly to the hard drive in real-time via an integrated imaging system created by Boulder Imaging (Boulder, CO).

Illumination is from a continuous Argon Ion laser running at 0.25 Watts running in a light-limited mode. The beam is turned into a planar light sheet via a scanning mirror or galvanometer (Cambridge Technologies, Cambridge MA, model 6650) and enters the tank through the free surface. This allows the possibility for free surface motions to distort the light sheet. Fortunately this effect is quite small, due to our low Reynolds number and the absence of facility-induced capillary waves. Future experiments will be in a tank with a transparent bottom through which the light sheet can be delivered.

The time series of imaging control described below is shown in Figure 2. The scanning mirror is driven with a sawtooth signal at 125 Hz. Except for the regions near the peaks of the curve, its motion is linear in mirror angle vs. time. During an experiment the laser and mirror run continuously, and an electronic shutter (NM Laser

Products, Sunnyvale CA, model LS200FNC) between them blocks the beam except when images are exposed. The first step of a measurement is to start the camera integrating with the shutter closed. The camera receives little to no light because the entire laboratory is kept dark. The shutter is then opened for ≈ 3 ms, during the linear part of the mirror's scan, to expose the first image. 7.92 ms after the shutter first opened to begin illuminating the first image, the mirror has completed one cycle, thus we can open the shutter again to illuminate a second image. During the ≈ 5 ms interval between illumination of the first and second images, the first image is closed and integration begun on a second image. This image pair can now be processed to find the concentration and velocity fields.

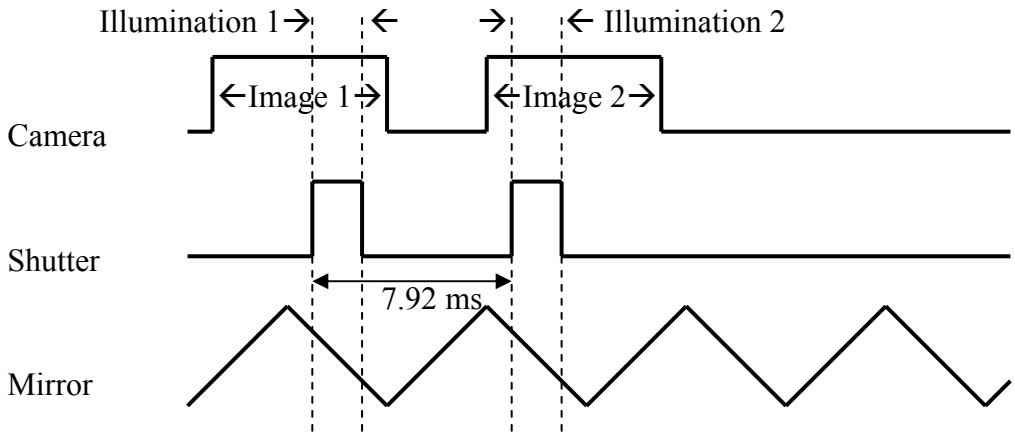

Figure 2. Time series for the capture of one image pair. Horizontal axis is time and vertical axis is voltage. High voltage corresponds to camera integration and open shutter, while voltage is proportional to angular position for the scanning mirror. Image pairs are recorded at 1.25 Hz.

Each image has a mean pixel value of ~500 counts, due almost entirely to the fluorescent dye mixed throughout the water. Before adding CO_2 gas to the system, a

series of images are taken to calculate a reference value at each pixel. After the CO_2 transfer begins, images will show some darker regions corresponding to areas of high CO_2 concentration and brighter spots corresponding to images of tracer particles. Because of this, the signals for PIV and LIF are separable – everything brighter than the reference value is a tracer for PIV and everything darker is our $[CO_2]$ measurement by LIF. In practice we do not do such a separation.

2.5 Free Surface location

Our image area includes the free surface, the location of which moves from image to image due to the effects of near-surface turbulent motions and unfortunate surface waves (discussed in section 3.2) that will be eliminated in future experiments. Because our camera's optical axis is beneath the free surface we see reflections of subsurface features in the region of the image above the free surface. These reflections can distort our PIV and LIF measurements, and so must be removed. To do so we must locate the free surface and discard all data above it.

One technique for doing this is to use a secondary camera to image the same region but with its optical axis above the free surface. The surface location will be obvious in such images, and can easily be found via digital image processing. The location can then be mapped onto the main images and used to remove the reflections above it (Banner and Peirson 1998).

A second technique is to identify the free surface location from the fact that it causes a reflection – we expect the free surface to be the line about which the image is symmetric. This technique is employed by Münsterer and Jähne (1998) and Herlina and Jirka (2004). We found that this method performed poorly because the reflected part of an image is not reflected exactly, but rather is compressed in the vertical direction and shows decreasing intensity with distance from the free surface. We

found it more accurate and less time consuming to identify the free surface location manually in each image, using Matlab code to make this process rigorous, repeatable, and relatively painless.

The free surface is essentially flat for the small image area and low-Re cases described here, but a wavy surface can be identified by manually finding the free surface at several points in each image and using 2D spline interpolation to infer the free surface between these points. Once the free surface is identified, the area above it is set to zero counts and the image is rewritten so that the free surface is at the same height in all images.

2.6 PIV

Velocity measurements are made using the PIV technique of Cowen and Monismith (1997). In brief, a velocity vector can be found at a point in a pair of images by considering two subregions near this point, one in the first image and one in the second image. The subregions are of identical size, and their locations are moved while the subimages they contain are correlated via one of several schemes. The subregion positions that correspond to the maximum correlation allow us to compute the 2D velocity vector at the point in question. Velocities are typically found at points on a grid; when this grid's spacing is smaller than the size of the subimages some data is being used twice, which means that neighboring velocity measurements are not completely independent. In the data reported here, the subregion size is twice that of the grid spacing, so a vector is independent from its second-nearest neighbors.

PIV is accomplished in a series of iterative passes, the results of each informing the next pass. After each pass bad vectors are identified and replaced with interpolated values. Refinements in each successive pass can include using a smaller subregion (size N pixels) to calculate particle position correlations, interrogation of

velocity vectors on a finer grid, or employing a more computationally expensive subpixel fit algorithm to find velocities that have non-integer values (in pixels/timestep). The data discussed here is processed as follows: Pass 1: N=64 pixels; Pass 2: N=40; Pass 3: refine grid from 64x64 to 32x32; Pass 4: apply Hart's error-correction algorithm (Hart 2000); Pass 5: N=32. Because tracer particles show up much brighter than the reference image (~2000 counts as compared to ~500), it is easy to identify these and create a particle-only image for PIV. However, PIV is successful when applied to our data as is, so this technique is not needed.

Filters must be used in PIV to reject inaccurate (bad) vectors suggested by spurious correlations, but also must be applied carefully so as not to obscure or erase real measured physics (throwing out the baby with the bathwater).

One filter used extensively in this work to identify bad vectors was a global filter based on the absolute correlation between the two subimages from which the velocity vector was inferred. If the correlation between the subimages is greater than T_C, the vector is considered valid.

Another filter option is the global variance filter, in which any velocity vector with a magnitude more than n standard deviations from the mean is deemed invalid. Since the standard deviation of the mean (σ) changes after these vectors have been discarded, this filter is iterated, either a fixed number of times or until no vectors are outside $n\sigma$ and thus σ ceases to change.

A third filter option is the local median filter, in which one computes the median velocity value in a neighborhood surrounding each grid point. If the velocity magnitude at this point differs from the local median by more than S (the units of which are pixels/timestep) then it is discarded. Since velocity values are ideally between 1 and 10 pixels per timestep (assuming a 32 pixel subregion) S is typically set around 5. If S is set too small then important features like filaments or sharp velocity

gradients can be discarded. In the data discussed here I used a conservative value of S=8.

In the data reported here, we apply the local median filter after each pass of PIV, and interpolate values for these vectors with a Delauney triangularization. After the final PIV pass, a correlation threshold filter was applied, and no interpolation was performed. Statistics were calculated only considering those vectors which passed the threshold. The threshold was typically set at 0.5, but relaxed in cases where more vectors were needed for statistics (primarily in calculations of the dissipation rate).

Recent analysis suggest that this type of filter may bias the velocity fields. Calculated values for both mean velocity and dissipation rate depend strongly on the correlation threshold, and do not converge as the threshold approaches either 1 or 0. RMS values such as U' and V' however, show weak dependence on T_C and do converge. Clearly further analysis is needed on the effects of this filter.

2.7 LIF

LIF is typically done by using the fluorescent dye itself as the scalar of interest, and measuring its concentration (via fluorescence intensity) as it mixes with clean water. Using pH-sensitive fluorescent dye that is mixed throughout a tank to identify local changes in pH was first done by Hiby *et al.* (1967). Several such techniques now exist, described in Jähne and Haußecker (1998). The method we use was optimized by Asher and Pankow (1986).

A major goal of ours is to measure the instantaneous mass flux <W'C'>. To get this right the concentration field must be imaged at same instant as the velocity field. Our LIF measurement must represent the concentration field at the time it is imaged, and not a delayed or time-integrated version of the concentration field. To

ensure this we consider the speed of the chemical and physical processes central to this technique.

Asher (1987) shows that the pH change from dissolving CO_2 can happen quite rapidly. He calculates that the pH can cover the entire dynamic range of this experiment (pH 8 to 4) in 100 ms, while a more typical change of 0.1 pH takes between 5 and 20 ms. The resulting change in fluorescence is due to pH-dependent changes in the conjugate acid/conjugate base speciation of the dye, whose less-fluorescent species dominate at lower pH values. This change in dye speciation is effectively instantaneous, being the timescale for protonation/deprotonation of a dye molecule (Bill Asher, personal communication). Thus our LIF technique is fast enough to resolve extreme concentration changes with timescales on the order of 100 ms seconds or longer, and minor concentration changes with timescales on the order of 10 ms or longer. Further, Soli and Byrne (2002) report CO_2 hydration constants greater than ~10 s^{-1}, indicating a timescale of 100 ms for pH changes do to CO_2 dissociation.

The diffusion timescale for the $[CO_2]$ concentration field is ℓ/D_{CO2}; setting the lengthscale ℓ to our resolution limit (the smallest lengthscale we can resolve corresponds to one pixel, which images an area of width 25.4 microns), we find the diffusion timescale is 350 ms. Comparing this to the dye response time upper limit of 100 seconds, we see that the fluorescent dye responds to even an extreme change in $[CO_2]$ before the CO_2 can diffuse across about 1/3 the length of a pixel. Concentration field evolution by diffusion is slow enough to be resolved accurately by our LIF technique. The effects of turbulence dominate diffusion except in the upper CBL, thus we must consider the timescales of turbulent motions as well.

The turbulence timescale for large eddies is $\tau = L/U'$, where L is the integral lengthscale; values which follow are taken from Figures 9 and 14. We find that in the

bulk fluid τ has a lower bound of τ_{bulk} = 80 ms. Near the surface, for eddy motions normal to the surface, $\tau_T = L_T/W'$ = 125 ms and for eddy motions parallel to the surface $\tau_L = L_L/U'$ = 60 ms. This makes sense because the free surface acts to increase the magnitude of horizontal velocity fluctuations at the expense of the vertical fluctuations.

The turbulence timescale for the smallest eddies in the flow is the Kolmogorov timescale $\tau_\eta = (\nu/\varepsilon)^{1/2}$ which is roughly (0.01 cm^2/s / 20 cm^2/s^3) $^{1/2}$ = 22 ms. However, the smallest motions we can resolve with our imaging setup are at the PIV resolution limit of 813 microns, roughly 8 times larger than the Kolmogorov lengthscale. If motions at this scale are in the inertial subrange (i.e. large enough to not be effected by viscosity), their timescale is given by $\tau = \tau_\eta (\ell/\eta)^{2/3}$ (Pope 2000, p.187). Examining the velocity spectra in Figure 11, the $\kappa^{-5/3}$ slope which is characteristic of the inertial subrange is present up to our highest resolved wavenumber, thus the assumption that our smallest resolved eddies are in the inertial subrange is a valid one, and we can compute τ_{small} = 90 ms.

Table 1. Timescales relevant in comparing our optical technique response time and the turbulent processes we wish to investigate.

Process	**Timescale**
pH change across entire dynamic range	100 ms
pH change of 0.1	5-20 ms
Molecular diffusion across one pixel	350 ms
Large turbulent eddy turnover (bulk)	80 ms
Large eddy turnover at surface (transverse)	125 ms
Large eddy turnover at surface (longitudinal)	60 ms
Smallest eddy turnover	22 ms
Smallest resolved eddy turnover	90 ms

In summary, the range of timescales for all resolved turbulent motions overlaps the range of dye response timescales significantly (see Table 1). Turbulent timescales are typically shorter than the dye response time for the most extreme concentration changes, but all turbulent timescales are longer than the dye response time for smaller, more typical concentration changes.

This equality of timescales could challenge our experimental technique, as a turbulent eddy injecting CO_2 into clean water could have a significantly different position, shape, or velocity by the time the dye has responded and shown that [CO_2] transfer has occurred. We saw this type of LIF response delay in a different experiment in which CO_2 bubbles rising from a needle at the base of a tank left a trail of decreased fluorescence, but the trail did not begin until several diameters behind each bubble, even though the gas transfer must have been happening right at the bubble surface. Luckily for this experiment, the CO_2 transfer is not occurring by

injection of pure CO_2 into clean water, but rather by the diffusion of CO_2 into a surface layer, and the mixing of fluid from this layer into the bulk. Strong viscous effects in the uppermost part of the CBL reduce the magnitude of velocities there, and the concentration changes are less abrupt than if turbulent eddies were able to approach the surface undamped. As a result, we expect the residence time of fluid in the CBL to be long compared with the dye response time. Turbulent motions transporting fluid from the CBL are transporting fluid in which the pH-induced fluorescence change has already occurred. Thus the fact that dye response timescales are on the order of turbulence timescales is a minor one, since the dye response has a significant "head start" due to the stagnant nature of the upper CBL.

2.8 Calibration

Because the relationship between fluorescence intensity and $[CO_2]$ is nonlinear, a multi-point calibration is necessary. To perform this calibration we need to measure pixel intensity at known values of $[CO_2]$. These reference values of $[CO_2]$ are difficult to obtain accurately, however. One method is to control the partial pressure of CO_2 in the headspace above the tank and use Henry's law to find the equilibrium bulk $[CO_2]$, and do so for several different partial pressures. This method is not ideal, however, as it is extremely slow, requiring roughly one day per data point, because it takes this long for the tank to reach equilibrium with the headspace.

The method we used involves gradually adding CO_2 by bubbling (to avoid a CBL) while keeping the tank well mixed. We measure the bulk concentration via two pH electrodes (Ross Orion combination electrode, Corning gel electrode) mounted ≈ 5 cm beneath the free surface. Given $pCO_2 = 1$ in the headspace we can compute bulk $[CO_2]$ from the pH readings as shown in Appendix A. We confirm the results obtained from the pH electrodes and these calculations with a commercial TIC (total

inorganic carbon) meter that strips all CO_2 from a water sample with strong acid and measures its concentration via a mass spectrometer (OI Corporation, College Station TX). Figure 3 shows excellent agreement between these two methods.

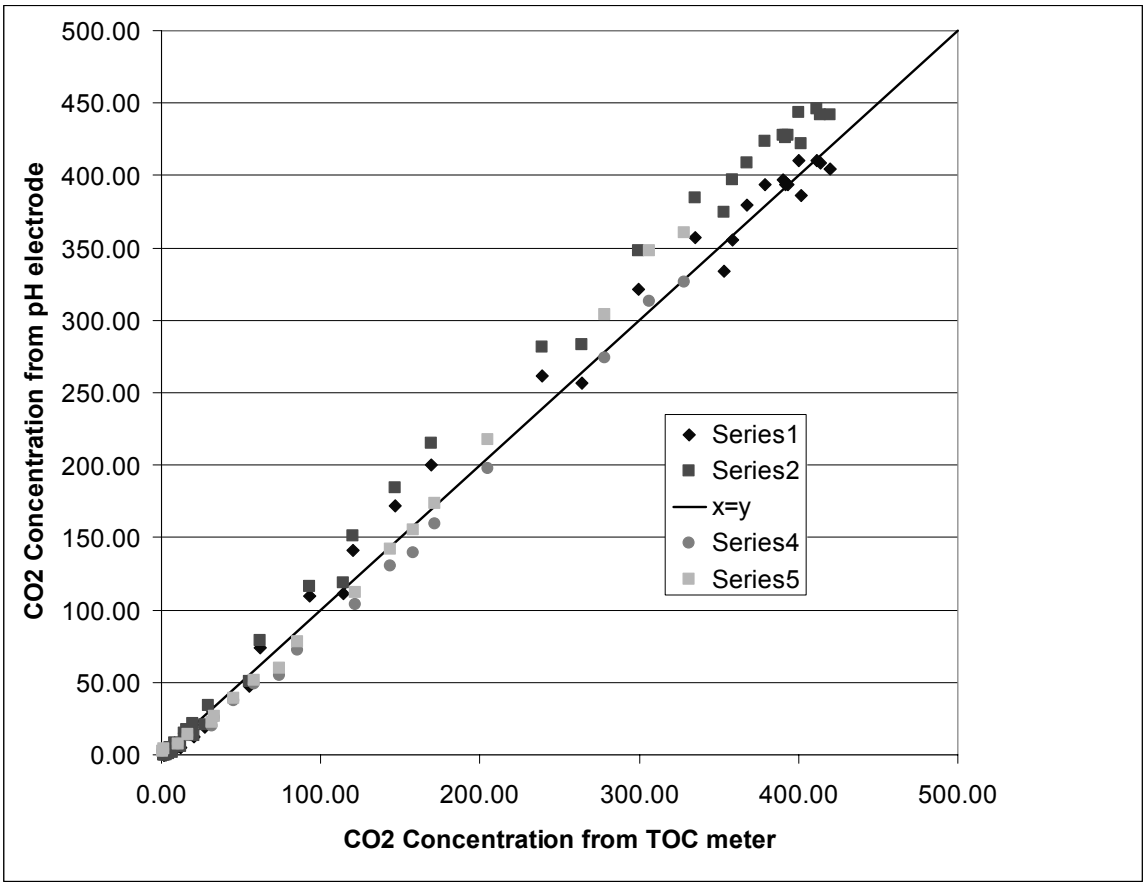

Figure 3. Calculations of bulk [CO_2] from pH measurements during four calibration experiments agree with the values of [CO_2] measured directly by a TOC meter in TIC mode.

While varying the bulk [CO_2] and measuring it via pH electrodes in this way, we simultaneously record pixel intensities with the same camera position and illumination conditions as the experiment itself. We vary [CO_2] so that fluorescence intensity covers the entire range observed in the experiments, giving a dynamic range of I* = [0.4, 1], pH = [3.9, 7], and [CO_2]=[0, 420 mg/L]. The highest [CO_2] measured

in our calibration or experiment (420 mg/L) is still much smaller than the saturation value of 1479 mg/L (Section 3.6). This is because it takes several hours to reach saturation, even with strong turbulent mixing. The [CO_2] range we measure in is ideal, because it corresponds closely to the pH range in which the dye response is strongest and in which the calculations converting pH to CO_2 are straightforward. A sample calibration curve is shown in Figure 4.

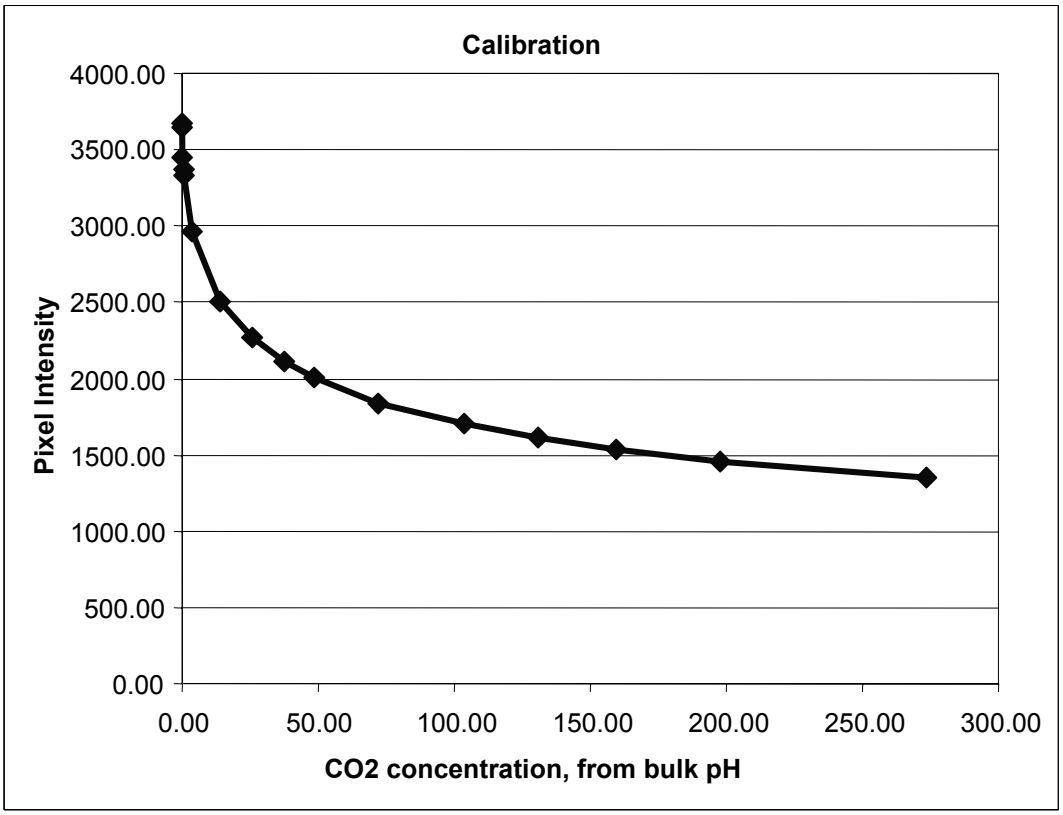

Figure 4. Sample calibration relating intensity at a single pixel to bulk [CO_2].

Uncertainty in this method comes from two sources, the measurement of pH and of fluorescence intensity (which includes variability in both illumination and recording). Uncertainty of each can be determined from the calibration experiments as follows. Consider a smooth section of the calibration time series for either bulk pH or

fluorescence intensity at a single pixel, then fit a curve to the time series trend and subtract this to find the residuals. A bootstrap analysis of these residuals gives the 95% confidence interval for that quantity. The uncertainty found in this way for pH can be propagated through the equations used to find $\delta[CO_2]$, giving a roughly 2% error in $[CO_2]$ for a pH uncertainty of 0.01. An initial attempt at this uncertainty analysis suggests a 3% error from pH measurement uncertainty and a 2% error in pixel intensity. These errors can be combined to find the uncertainty in our calibration curve via bootstrap. Uncertainties of this magnitude are acceptable for resolving the mass flux effects described below.

Once we have a calibration dataset we can apply the direct or nondimensional calibrations to each pixel. To apply a nondimensional calibration, we hypothesize that each pixel exhibits its maximum intensity at the highest pH value (lowest $[CO_2]$); this value occurs at the start of the experiment before CO_2 transfer begins. Recall that the intensity change with pH is due to a change in the species ratio of the fluorescent dye, and at uniform $[CO_2]$ this species ratio change should be the same at every pixel. Thus we hypothesize that at a given pH, every pixel will have lost the same fraction of its maximum (initial) intensity. Thus we attempt to nondimensionalize instantaneous pixel values by the reference image, created by ensemble averaging the first 10 images of the experiment. Thus we measure intensity as $I^* \equiv I/I_0$. Calibration experiments support our hypothesis, showing good collapse of I^* vs $[CO_2]$ for different values of laser power, DCF dye concentration, and pH of the water before CO_2 transfer begins. This is seen in Figure 5. However, these nondimensional curves do not collapse when compared from pixel to pixel, showing variations in I^* of up to 5%. This supports performing a per-pixel direct calibration, where a separate curve is fit at every pixel to describe the relationship between absolute intensity and $[CO_2]$ there.

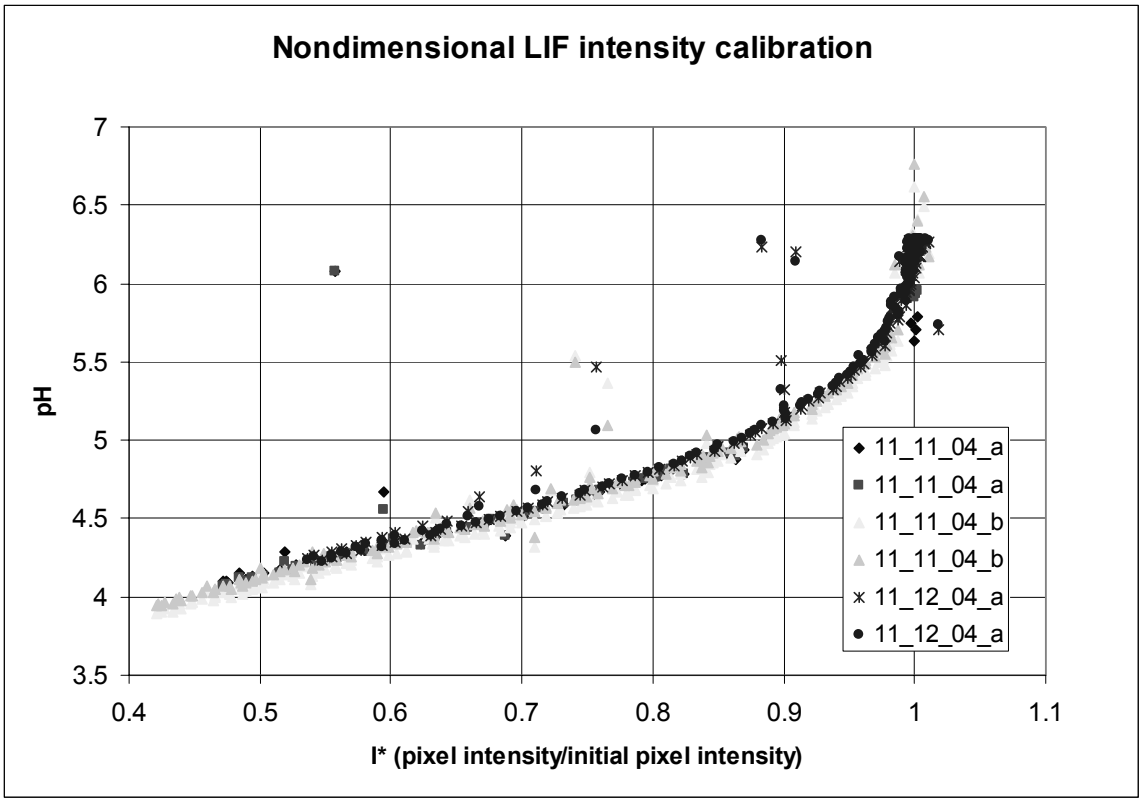

Figure 5. Nondimensional calibration curve at a single pixel for three runs and two pH electrodes. Spurious points correspond to shadows from contaminant particles covering the pixel, giving temporarily decreased I* values.

Different pixels have different gains and offsets, and are effected to different degrees by lens vignetting, laser beam intensity attenuation by dye, and illumination differences as the scanning mirror gives a position-dependent beam velocity. The nondimesional calibration corrects for these effects automatically when each image is divided by the reference image. The direct per-pixel calibration also takes these effects into account – they are the reason why each pixel has a different calibration curve, and by calibrating each pixel separately we address all of these effects.

The data discussed in the next section was calibrated with a global non-dimensional calibration, not the preferred per-pixel direct calibration. This has the

effect of increasing uncertainty, as pixel-to-pixel variations in the nondimensional calibration curve means that any I* value corresponds to a broader range of $[CO_2]$ values than the range implied only by uncertainty in pH measurements.

2.9 Coupling PIV and LIF

PIV will give us the central-difference estimate of velocity at the instant halfway between the first and second images. LIF will give us the concentration fields at the moments the images are taken. Thus if image 1 is taken at time t=0, and image 2 at time Δt, we have concentration fields at $t = 0$ and $t = \Delta t$, while our velocity field is at $t = \Delta t/2$. This begs the question of how to best correlate the concentration and velocity fields. Other implementations of single camera coupled LIF-PIV take three images, using the first and third to calculate velocity fields and the second to give the concentration field (Cowen *et al*. 2001). The difficulty with this technique is that it takes significantly longer to collect an image triple than an image pair, thus one needs a high speed camera or a flow with low turbulence levels so that particle positions can be correlated after a longer time interval.

It is possible that at the resolution of our velocity field measurements, the concentration field is stationary over Δt, which is set so that fluid velocities are less than 10 pixels in any timestep. As we saw above, molecular diffusion will not measurably effect the concentration field over this time interval. Thus we expect the concentration field to follow the velocity field and move by less than 10 pixels in any timestep. PIV velocities are spatial average velocities over a 32x32 pixel region. Our hope is that 10 pixel motions of the concentration field are negligible when averaged over a 32x32 pixel region. We test this by undersampling and smoothing the concentration field, computing the median concentration over 32x32 pixel regions centered on the velocity field grid points. Unfortunately, the undersampled

concentration fields still change visibly over Δt, as seen in Figure 6, thus the timing problem must be dealt with.

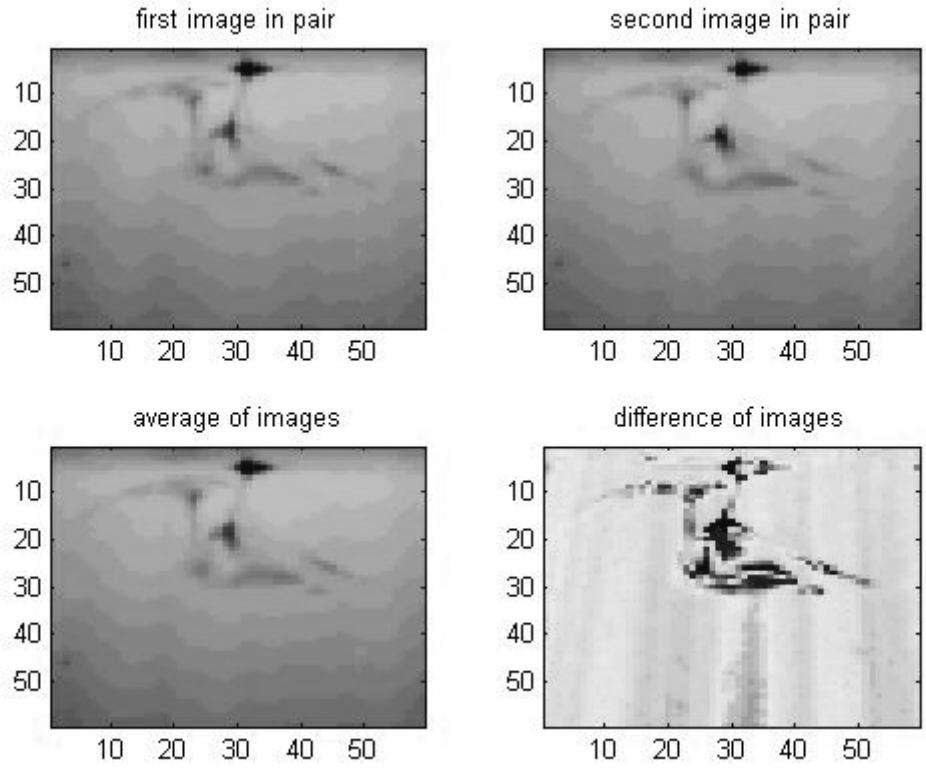

Figure 6. Uncalibrated undersampled images, showing median pixel intensity in 32x32 pixel subregions centered on the velocity field's grid points. Color scale in (a) through (c) is [200, 1000] counts per pixel, and [-10, 10] counts/pixel in (d).

One option for resolving this timing problem is to use the average of the two concentration fields. This is not ideal, as a single feature becomes a pair of features, which could distort the physics we are investigating.

Another method is to use the measured velocity field to artificially advect the first concentration field forward in time and the second field backward in time, taking the average of these values. This seems like the most rigorous solution, and will be implemented in future work. Due to the PIV resolution limit we would have to perform this method on the undersampled [CO_2] field.

The method used for the mass flux data reported here is to simply use the first image in each pair. I do not expect this choice to cause qualitative changes in our results. We should repeat these calculations using the second images from each pair, and calculate the uncertainty from differences in the instantaneous mass flux.

In the data reported here, concentration fields were undersampled differently than described above. With the intention of preserving information about small structures such as filaments, and to keep neighboring concentration measurements independent, we compute the median concentration over 3x3 pixel regions centered on the velocity field grid points, rather than the 32x32 regions described above. This method provides much better visibility of the CBL, as seen in Figure 7.

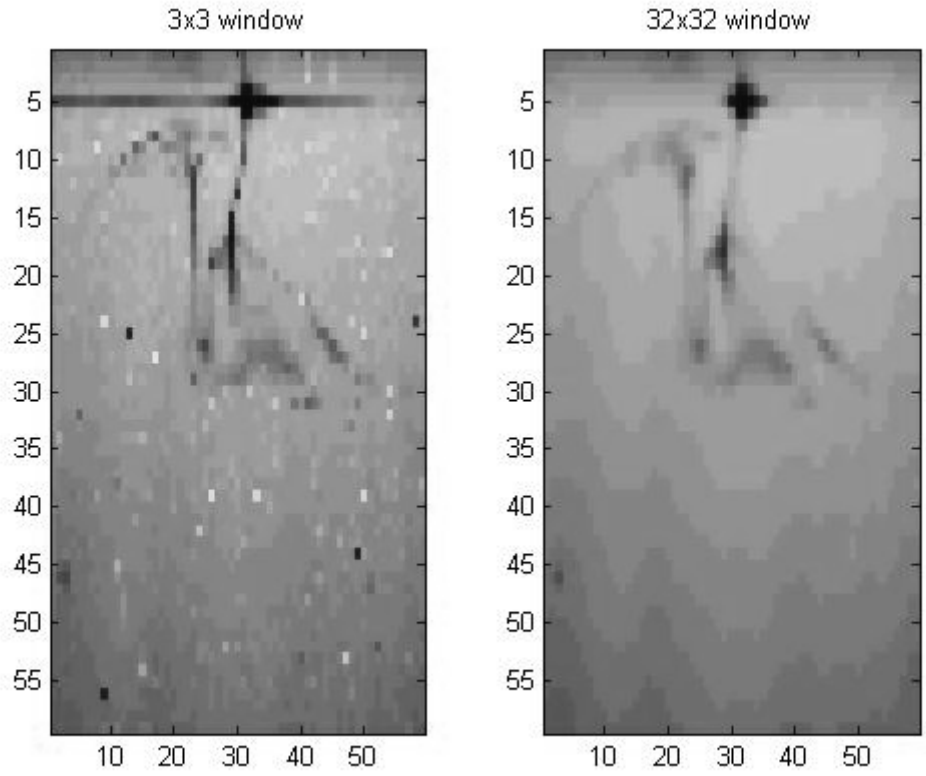

Figure 7. Uncalibrated undersampled images, showing median pixel intensity in subregions centered on the velocity field's grid points**.** Subregions are 3x3 pixels in (a) and 32x32 pixels in (b).

CHAPTER 3

RESULTS

3.1 Mean and Fluctuating values

The mean velocity at each PIV grid point was found by ensemble averaging across our 500 samples, and is denoted by <U>. The median velocity values at each point are denoted U_{med}. The instantaneous fluctuating values are denoted $U' = \langle (U - \langle U \rangle)^2 \rangle^{1/2}$. The median velocity field was nearly identical to the mean, but for completeness we also calculate $U'_{med} = \langle (U - U_{med})^2 \rangle^{1/2}$ We use both U' and U'_{med} in all calculations, and if there is no qualitative difference, the values based on U' are used.

Because the concentration time series at any point is non-ergodic ($[CO_2]$ is increasing throughout the experiment, see figure 10) we cannot find the fluctuating values by simply subtracting a time-averaged mean value. Rather, we consider the horizontally averaged concentration at each depth over time. We fit a curve to this time series, $\underline{C}(z,t)$ which we consider the average concentration as a function of depth and time. Thus for any instantaneous pixel value C(x,z,t) we define $C'(x,z,t) \equiv C(x,z,t) - \underline{C}(z,t)$.

C'(x,z,t) can be multiplied by W'(x,z,t) to find the instantaneous scalar flux F(x,z,t). A negative value indicates transfer of CO_2 from the gas phase to the water. The horizontally averaged instantaneous mass flux near the surface F(z = 0.6 cm,t) is seen in Figure 17a. The same quantity can be measured from the time rate of change of the bulk concentration, $F(t) = (\forall/A)*dC_{bulk}(t)/dt$, where $\forall$ = tank volume and A = free surface area. Comparing these two measurements (which are independent other than sharing the $[CO_2]$ calibration curve) of flux will help to confirm the accuracy of our measurements. As seen in the Figure 8b, these two values show excellent agreement over the duration of the experiment.

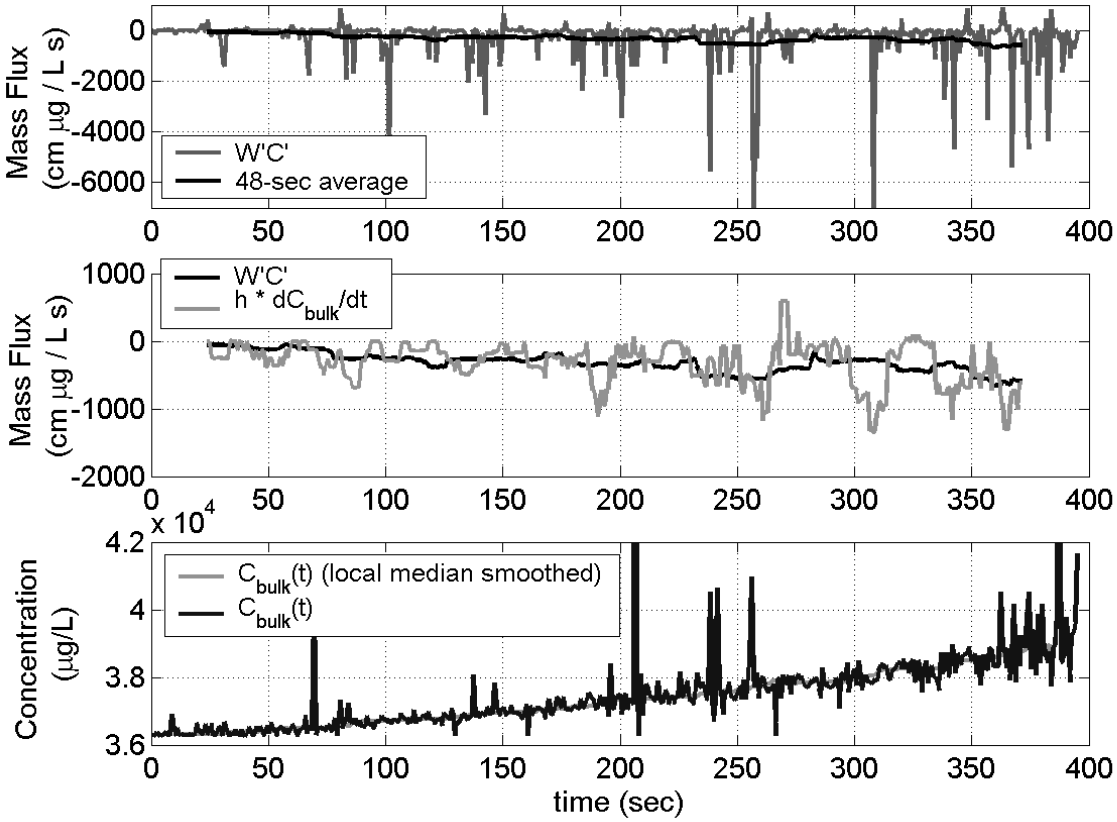

Figure 8. **(a)** W'C' horizontally averaged at the measurement depth closest to the surface (0.6 cm), peaks are smoothed away with a 48-second running average to show the underlying trend. **(b)** Two measures of mass flux: smoothed W'C' curve from (a) and time rate of change of smoothed bulk [CO_2] curve from (c). The latter is calculated with a simple finite difference method, dC_{bulk}/dt = C(t+4 sec)-C(t-4 sec)/8 sec. **(c)** Bulk [CO_2] from median LIF values over 3x3 pixel window. Peaks correspond to shadows and particles as discussed in Figure 5, thus we smooth this curve with a local median filter.

3.2 Vertical profiles

Profiles of turbulent velocity statistics, seen in Figure 9, include U', W', and mean turbulent kinetic energy, $k = 0.5 * (U'^2 + V'^2 + W'^2)$ calculated with the symmetry assumption V' = W'. All quantities are averaged horizontally (parallel to the surface) and across time. Away from the free surface we see k decreasing with distance from the synthetic jet array, indicating decay of the turbulent energy with distance from the turbulent source, as expected. Closer to the surface, we see W' decreasing more sharply as the surface is approached, while U' begins to increase. This is due to a transfer of energy from W' to U' superimposed on the turbulent energy decay. Vertical motions are suppressed by the free surface, and this energy is transferred to horizontal velocity fluctuations. The depth at which this transfer begins is obscured in this dataset by a third process affecting the velocity fields, discussed below.

Energy is being added at the surface, clearly seen in the near-surface increase in k. Two possible causes are surface gravity waves or compressional waves along an elastic surfactant layer. Periodic surface height variations can be clearly seen in a time series of free surface height, and have a period of T=3.8 seconds. Shallow water wave theory gives us a corresponding wavelength, $\lambda = T(gh)^{1/2} = 6.9$ meters for this case. This is much larger than the tank width of 15.4 cm, which makes it unlikely for the free surface fluctuations to be from gravity waves. They could be caused by fluctuating storage due to air pockets in the pump or manifold driving the turbulence, giving a periodic net change in tank volume. There is no straightforward way to calculate the surface energy profile due to such volume variations, surfactant waves, or even deep water gravity waves. In future experiments we will measure energy profiles before and after surface cleaning, to test the existence of the hypothesized surfactant waves. Furthermore, we will use two acoustic wave gauges to obtain higher

frequency surface height measurements and provide a synoptic measurement of free surface height at two locations separated by more than the 2 cm provided by our imaging system. We could also attempt to isolate the wave motions by measuring surface motions after the turbulence generator has been turned off; this will only work if the wave energy decays significantly slower than turbulent energy. Should surface waves be a problem in our full-size facility, it has a large enough surface area that we can add a floating baffle surrounding the measurement area to absorb wave energy.

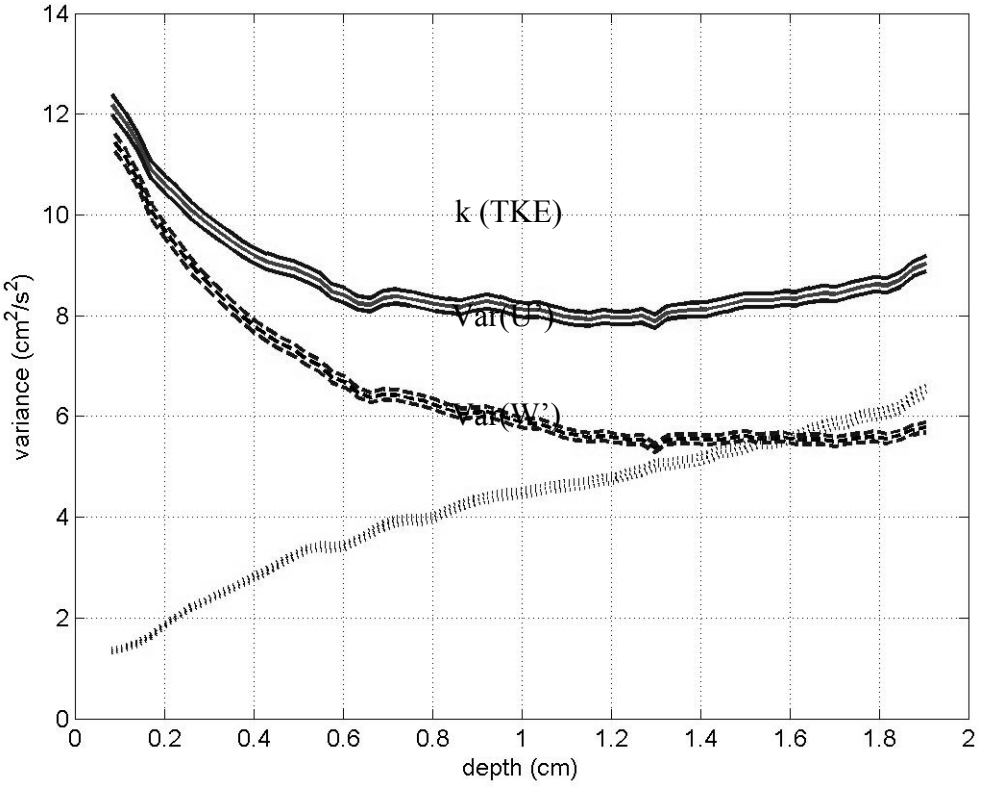

Figure 9. Turbulent velocity profiles. 95% Confidence Intervals via Bootstrap.

Vertical profiles of concentration over time show the evolution of the CBL, as seen in Figure 10. Attempts to nondimensionalize these curves with several different schemes based on surface concentration, initial concentration, mean concentration, and boundary layer depth were unsuccessful.

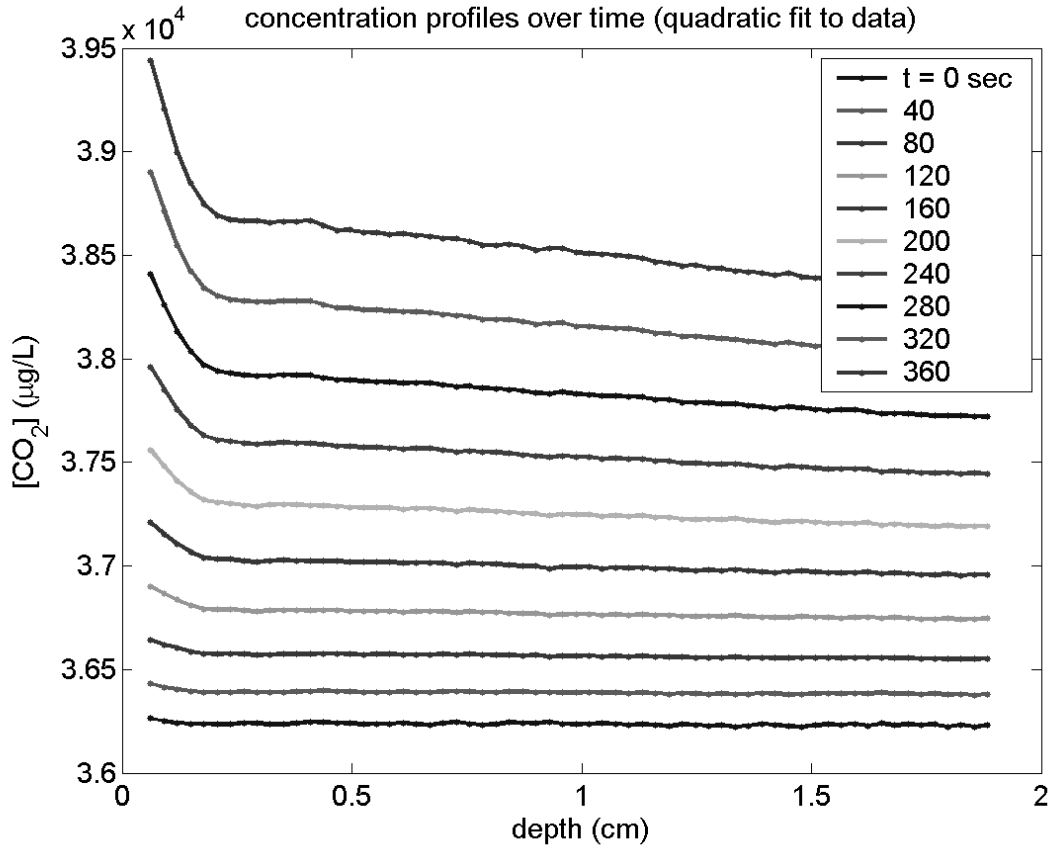

Figure 10. Concentration profiles over time (start of the experiment is the lowest curve). Curves are smooth because they are quadratic fits to the data.

3.3 Power Spectra

Spatial power spectra were determined for horizontal transects (parallel to free surface) at different depths and ensemble averaged over all times at a given depth. Spectra were computed for U' (longitudinal) and W' (transverse) as well as C'. All three spectra exhibit the expected slope of wavenumber to the -5/3 power, which shows that turbulence is dominating this system. The transverse power spectrum demonstrates the effect of the free surface on the vertical velocity W', namely that as we approach the free surface, vertical motions are reduced. The largest size features (lowest wavenumbers) are the first to be effected, which can be seen in the loss of energy at first low, and then progressively higher wavenumbers as the depth at which the spectrum is measured decreases.

Figure 11. Longitudinal (E_{11}) and Transverse (E_{12}) Power Spectra for the velocity fluctuation vectors U' and W' along a line parallel to the free surface, ensemble averaged over time. The shallowest measurement is denoted by circles. Depths are 0.9, 1.5, 2.1, 2.6, 3.2, and 3.8 mm below free surface.

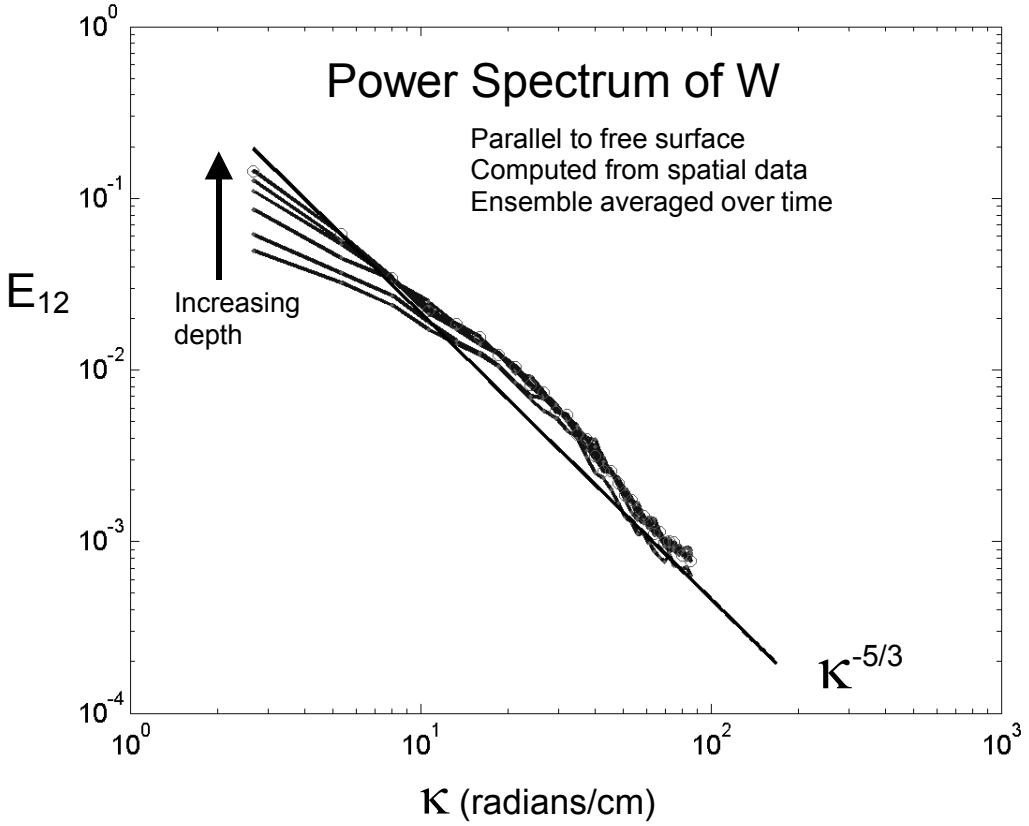
Power Spectrum of W
Parallel to free surface
Computed from spatial data
Ensemble averaged over time
Increasing depth
E12
κ-5/3
κ (radians/cm)

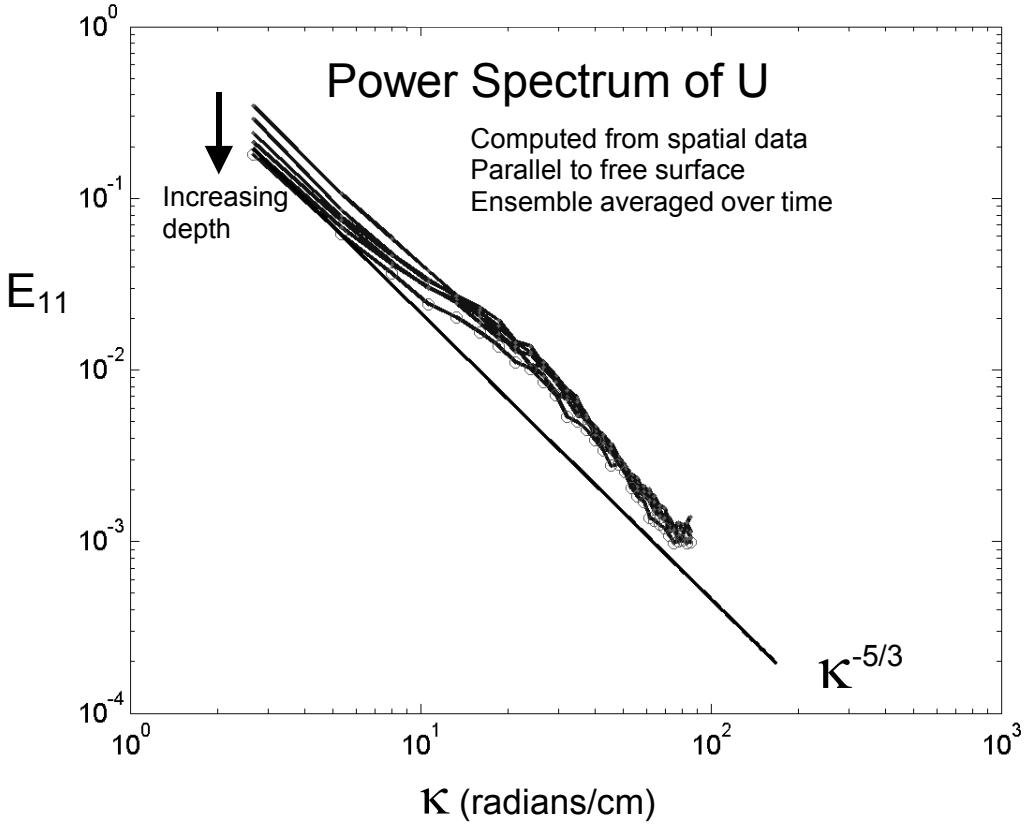
Power Spectrum of U
Computed from spatial data
Parallel to free surface
Ensemble averaged over time
Increasing depth
E11
κ-5/3
κ (radians/cm)

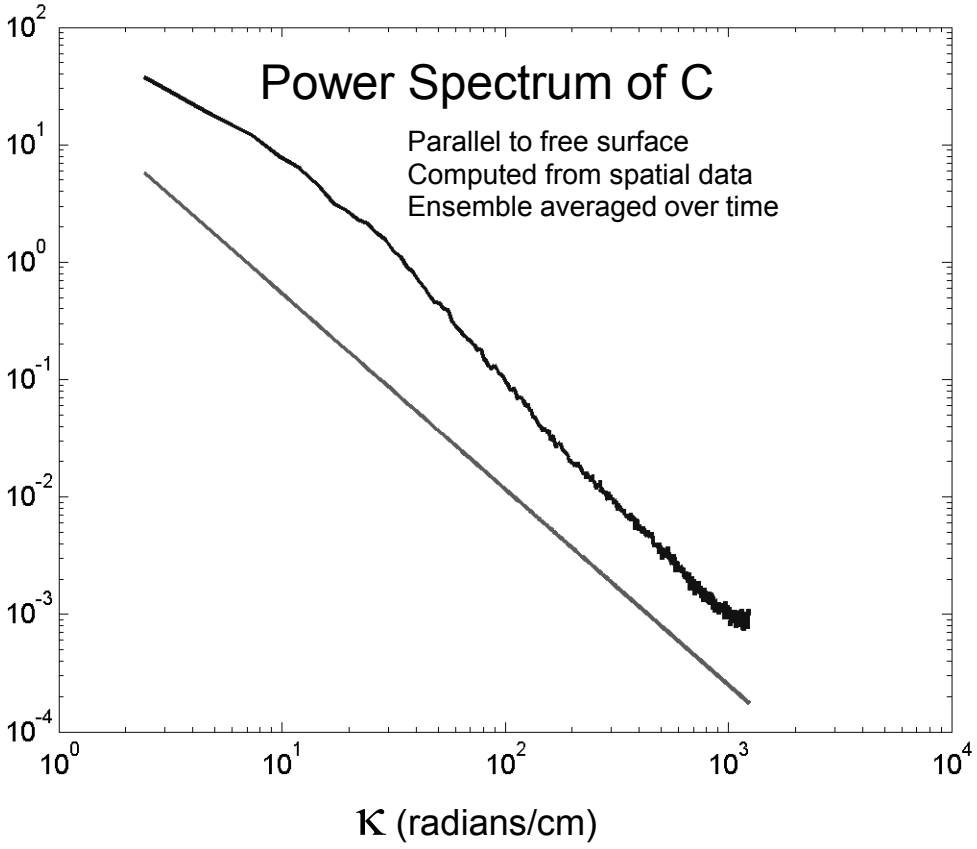

Figure 12. Power spectrum for fluctuating [CO_2] values along a line parallel to the free surface, ensemble averaged over time. Wavenumber range is higher than in Figure 11 because concentration field resolution (1 pixel) is finer than velocity field resolution (32 pixels). Y axis units are the fraction of the total variance in C' corresponding to features of wavenumber κ.

It is difficult to determine the form of the background noise that typically composes part of a power spectrum. We estimate the noise spectrum for our measurement of C' at the free surface by noting that at the greatest depths measured the mass flux is zero and C' remains small and constant with depth, likely being a product of noise alone. We consider the horizontal spectrum in the bulk as a measure of the noise spectrum for C' and subtract it from our computed surface-level C' spectrum.

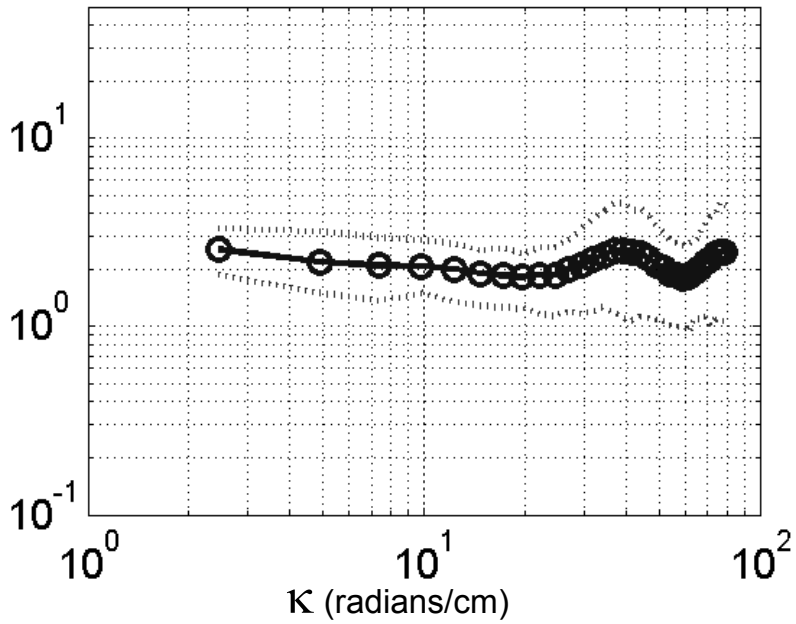

Figure 13. Power spectrum for mass flux (W'C') values along a line parallel to the free surface at the shallowest depth measured, ensemble averaged over time. Y axis units are the fraction of the total variance in W'C' corresponding to features of wavenumber κ. Dashed lines correspond to 95% confidence interval from bootstrap.

We also compute the power spectrum of the mass flux W'C' in the horizontal transect closest to the surface. We can estimate the noise spectrum for this data by

creating a false mass flux time series by multiplying W'(x,y,t) by C'(x,y,t+1). This spectrum should have the same noise features as the true mass flux, with none of the real physics. Thus we can consider the spectrum of this time series a good measure of the noise and subtract it from the spectrum of the true mass flux time series. The true spectrum exhibits higher amplitude than the noise, the median signal to noise ratio across wavenumber being 5.7.

Since both C' and W' have -5/3 spectra, it is surprising that their instantaneous products exhibit the nearly flat spectrum seen in Figure 13. The explanation is that compared to either W' or C', the product of these two signals has more fluctuations at small spatial scales *relative to* the number of fluctuations at large spatial scales. Both individual signals are dominated by large scale fluctuations, but in multiplying them one creates more fluctuations at smaller scales, which acts to "lift" the high wavenumber side of the spectrum. We can confirm this behavior by examining W', C', and W'C' values parallel to and just beneath the free surface under high- and low-pass spatial filters. The low-pass filter is a simple running average, and the high pass filter is the original signal minus the low-pass filtered version. For each signal we find the variance over space, and ensemble average these values over time. The results are seen in Table 2 and show a clear increase in high-wavenumber variance compared to low-wavenumber variance when W' and C' are multiplied.

The implication of this flat mass flux spectrum is that motions of many different sizes (~50 microns to ~4 cm) have an equally strong effect on gas transfer. As discussed in section 1.7.a, it is still an open question as to which size motions dominate mass transfer. Our result can help explain why SR theories based only on small or large eddies give results that agree well with each other and with experiment. If the mass flux spectrum is flat, then both SR models parameterize gas transfer based on features with equally strong effects.

Table 2. Comparing variances of velocity and mass flux time series confirms the flattening of mass flux spectrum seen when comparing Figures 11, 12, and 13.

Quantity	**Variance of Low-pass filtered signal**	**Variance of High-pass filtered signal**	**Ratio (high/low)**
W’	0.74	0.23	0.31
C’	9.09E6	2.78E6	0.31
W’C’	4.13E6	2.08E6	0.50

3.4 Integral Lengthscales

We find the integral lengthscales by directly computing the instantaneous spatial autocorrelation functions along horizontal transects at different depths. This gives the vertical profiles of integral lengthscales seen in Figure 14. Note once again that the longitudinal turbulent motions (U’) are essentially unaffected by the surface, while the vertical motions are reduced in size as they approach the surface – only small eddies, with small autocorrelation distances, survive near the surface.

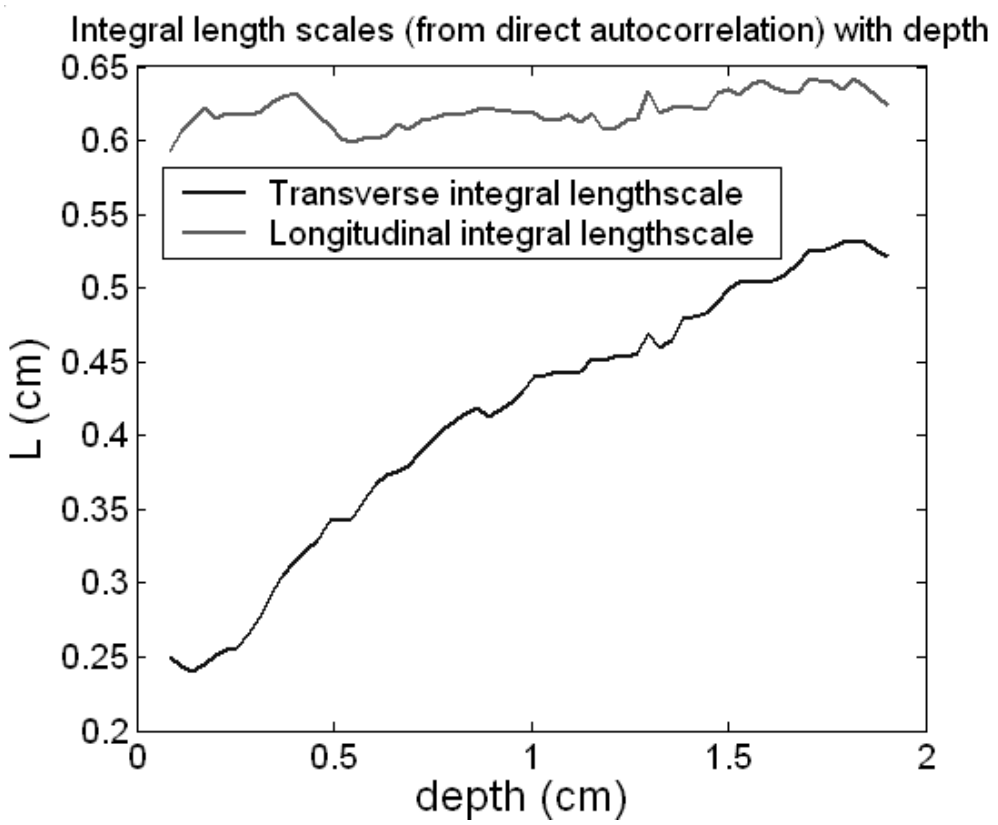

Figure 14. Vertical profiles of integral lengthscales.

3.5 Dissipation

Calculating the energy dissipation rate ε from PIV data is challenging and prone to large uncertainties. Nonetheless we attempt to find it here, as even rough values can be informative and motivate improvements for future analyses. Dissipation rate is central to Lamont and Scott's parameterization of gas transfer rate, yet most experiments attempting to verify their work must compute ε from other parameterizations or scaling arguments.

The dissipation rate should increase near the surface because of the extra TKE being inserted there by waves or surfactant effects (discussed in Section 3.2). One method of calculating ε uses the values of k, namely $\varepsilon = k^{3/2}/L$. Using k values from

Figure 9 and L_T values from Figure 14, this relation gives us 48 cm^2/s^3 near the surface and 16 cm^2/s^3 in the bulk. We can also approximate epsilon from the power spectrum, because in the inertial subrange we expect $S_{uu}\kappa^{5/3} = 0.25\varepsilon^{2/3}$ (Tennekes and Lumley 1973). Plotting the LHS of this equation and fitting to the flat section allows us to find an approximate dissipation rate, though this method typically overestimates dissipation (Doron *et al.* 2001) and is thus best as an order of magnitude check. We find 66 and 181 cm^2/s^3 from the transverse and longitudinal spectra, respectively. The values based on the longitudinal spectrum decreased with depth to a bulk value of 34 cm^2/s^3, while the transverse values remained constant.

The dissipation rate can also be calculated direct from its definition:

$$\varepsilon = -2\nu\langle S_{ij}S_{ij}\rangle = \nu\langle \partial u_i/\partial u_j(\partial u_i/\partial x_j+\partial u_j/\partial x_i)\rangle,$$

where <> represent time averages (Pope 2000, p.127). PIV measurements give us instantaneous values for the gradients du/dz, du/dx, and dw/dx, and dw/dz, from which mean gradients are calculated. The other needed gradients can be approximated (as instantaneous or mean values) from continuity and the x-y symmetry of our flow (Doron *et al*. 2001). Approximations for the two cross terms are the least well-founded, but luckily all 4 measured cross terms from which they are approximated have negligible magnitudes compared to other terms, meaning that a poor approximation will have little effect.

Table 3. Mean gradient approximations from symmetry and continuity used in direct calculation of the dissipation rate.

Unmeasured gradient	**Approximation**
$\langle(\partial u/\partial y)^2\rangle$	$\langle(\partial u/\partial x)^2\rangle$
$\langle(\partial v/\partial x)^2\rangle$	$\langle(\partial u/\partial x)^2\rangle$
$\langle(\partial v/\partial y)^2\rangle$	$\langle(\partial u/\partial x)^2\rangle + \langle(\partial w/\partial z)^2\rangle + 2\langle(\partial u/\partial x)(\partial w/\partial z)\rangle$
$\langle(\partial v/\partial z)^2\rangle$	$\langle(\partial u/\partial z)^2\rangle$
$\langle(\partial w/\partial y)^2\rangle$	$\langle(\partial w/\partial x)^2\rangle$
$\langle(\partial u/\partial y)\,(\partial v/\partial x)\rangle$	$\langle(\partial u/\partial x)\,(\partial w/\partial x)\rangle$ or $\langle(\partial u/\partial z)\,(\partial w/\partial x)\rangle$
$\langle(\partial v/\partial z)\,(\partial w/\partial y)\rangle$	or $\langle(\partial u/\partial x)\,(\partial w/\partial z)\rangle$ or $\langle(\partial u/\partial z)\,(\partial w/\partial x)\rangle$

Local gradients are calculated by a finite difference scheme, with Δx found adaptively so as to include most motions in the dissipation range (Cowen and Monismith 1997). We use gradients in U', as gradients in U will be artificially increased if there is any spatially varying mean background flow. Also, we only consider points at which the gradient is well-defined. Thus any point which has neighboring bad vectors is excluded from the dissipation calculation. The results are quite sensitive to the correlation threshold used to identify bad vectors. With no filter on at all, $\varepsilon = 60$ cm^2/s^3 while applying the filter with $C_T = 0.5$ gives a value of 20 cm^2/s^3. In both cases the vertical profile shows a decrease with depth, falling ~25% over the first centimeter.

3.6 Gas transfer velocity

The mass flux $F=(V/A)*dC_{bulk}/dt$ can also be written as the product of a transfer velocity K and a forcing term $\Delta C = C_{sat} - C_{bulk}$. Like many previous experiments we can compute the spatiotemporal average transfer velocity from our measurements of dC_{bulk}/dt. Integrating $(V/A)*dC_{bulk}/dt = K(C_{sat} - C_{bulk})$ we find $\ln(C_{sat} - C_{bulk}(t)) = -kAt/V + \ln(C_{sat} - C_{bulk\_initial})$, thus we can measure KA/V from the slope of $\ln(C_{sat} - C_{bulk})$ vs time. C_{sat} is the saturation value of CO_2 in water, or 1479 mg/L, as found from Henry's law: $C_{sat} = pCO_2/K_H$, where $pCO_2 = 1$ in our case because the headspace is pure CO_2 and K_H is the Henry's law constant for CO_2 gas, 29.76 atm/mol/L.

We find from our experiment K = 1.0 cm/hr; future experiments will be important to confirm this and determine uncertainty. For now, we confirm this value from our data using the scaling relation $K = D_{CO2}/\delta$ where D is molecular diffusivity and δ is the thickness of the CBL. Using Münsterer and Jähne's definition for δ, we find $\delta = 0.25$ cm from Figure 10, giving us K = 0.25 cm/hr. Herlina and Jirka (2004) show that K values measured in this way are typically less than those measured from bulk concentration changes.

Values of K for scalars with different diffusivities (a and b) can be compared via a Schmidt number scaling $K_a=K_b(Sc_a/Sc_b)^{-1/2}$. Typically, K values are compared at a Schmidt number of 600. Since CO_2 has a Schmidt number of 568, $K_{600}=0.97$ K_{CO2} similarly for O2 $K_{600}=0.83$ K_{O2}. Table 4 shows measured values for K_{600} reported in the literature for turbulence levels equivalent to those in our experiment. Also included are predictions from parameterizations - Fortescue and Pearson (1967) give $K = 1.46(2Dk^{½} / L)^{½}$ where k is turbulent kinetic energy $k = 0.5 * (U'^2 + V'^2 + W'^2)$. Lamont and Scott (1970) give $K = 0.4(\varepsilon\nu)^{¼} Sc^{-½}$.

Table 4. Gas transfer velocities from several experiments and parameterizations at Reynolds numbers close to ours. Much more data on K exists, but at a variety of Re. This subset is considered specifically to show the variability in K between measurements. At the time of writing, I am trying to resolve a contradiction between my calculated values of the Lamont and Scott and Fortescue and Pearson values (shown here) and McKenna and McGillis' calculations of the same, which give the more central value 6 cm/hr for both parameterizations.

k_{600} (cm/hr)	**Source**
0.97	This study
2	Chu and Jirka (1992)
3-7	McKenna and McGillis (2000)
30	Asher and Pankow (1986)
40	Lamont and Scott (1970)
65	Fortescue and Pearson (1967)

Given the wide range of values seen in Table 4, we note that our value is the same order of magnitude as the others, but on the lowest end of the distribution. Two possible reasons for our low K value will be investigated in future experiments. First, surface contamination can cause an order of magnitude decrease in K, as shown by

Asher and Pankow (1986). We can measure mass flux before and after skimming, to determine whether it is effectively reducing the surfactant layer. Second, our tank has been designed to reduce secondary flows, flows which are present in all other experiments and can greatly increase K. We can systematically measure the effects of such a secondary flow by adding toroidal convection to our turbulence pattern via a permanent synthetic jet (with adjustable flowrate) at the tank center, determining how much transfer in these cases is due not to turbulence but rather to secondary flows.

3.7 Features in the 2D instantaneous Mass Flux fields

Our coupled PIV-LIF technique gives us a timeseries of instantaneous mass flux values in a 2D plane. This allows for some measurements that have not been done before, such as the mass flux spectrum described in Section 3.3. It also affords a window into the fundamental physics of how mass transfer occurs.

One major feature we observe is visually striking mass injection events, such as that in Figure 15. In such events the CBL is pulled down into the fluid and then sheared away. We often see the shearing in process, such as on the RHS of Figure 15b, which also shows that these events can be rather large. A crude measurement of the event size is the width at a given depth. Measuring this size for the ~300 events observed in our 500 samples over 6 minutes, we find a unimodal distribution, peaked near the event size seen in Figure 15a. The distribution has a long tail which continues to the largest events observable in our field of view. This tail may follow a power law, but further data and a more robust size metric is needed before this can be verified.

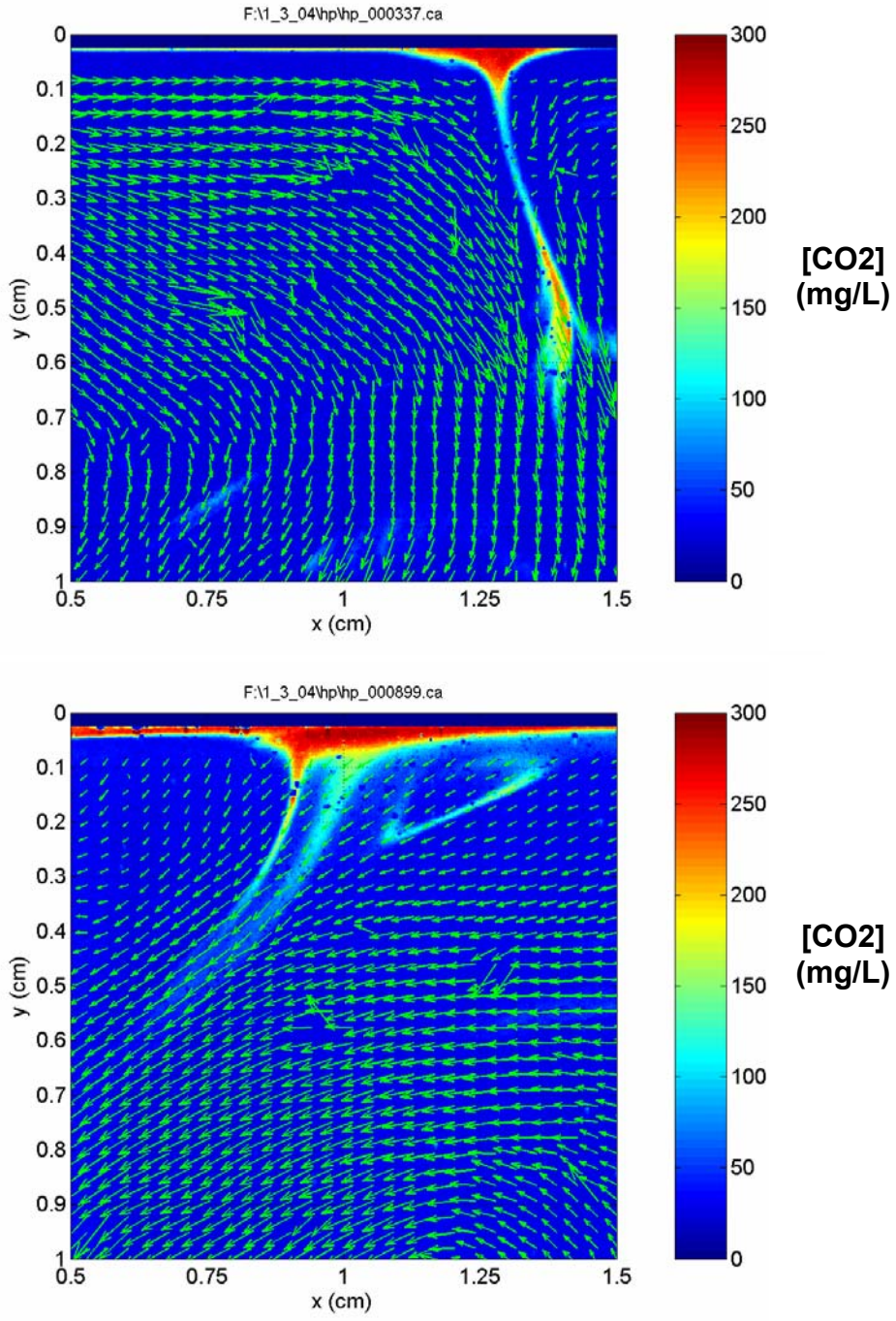

Figure 15. Instantaneous concentration and velocity fields showing mass injection events in which downward-moving fluid drags fluid from the CBL into the bulk, where it is sheared away.

These injection events are clearly being effected by turbulence, displaying a multi-scale structure of widths ~ η and lengths ~ L. Visually they seem to be correlated with downward going fluid motion, and this is confirmed by the mass flux signal at these times. Points inside these mass injection events have a signal of W'C'< 0, as W' is negative (downward-going) and C is larger than the typical value at that point. Negative mass flux represents transfer into the fluid, and can also be accomplished by upward-moving fluid with low [CO_2]. Such events are the surface renewal eddies hypothesized by Dankwerts (1951) and have been a major focus of gas transfer research. Their mass transfer signal is more diffuse than the mass injection events, but can still be clearly seen in Figure 16.

Since both types of events – surface injection and surface renewal – events have clear signals of mass flux into the fluid, we can compare them by dividing the observed instances of negative W'C' into those with W' > 0 and those with W' < 0. Figure 17 shows time series of instantaneous mass flux horizontally averaged across the depth closest to the surface, conditioned on the sign of W'. Summing the mass flux in each of these time series shows that the injection events (those with downwelling flow) are responsible for 8 times more mass flux than the surface renewals (upwellings).

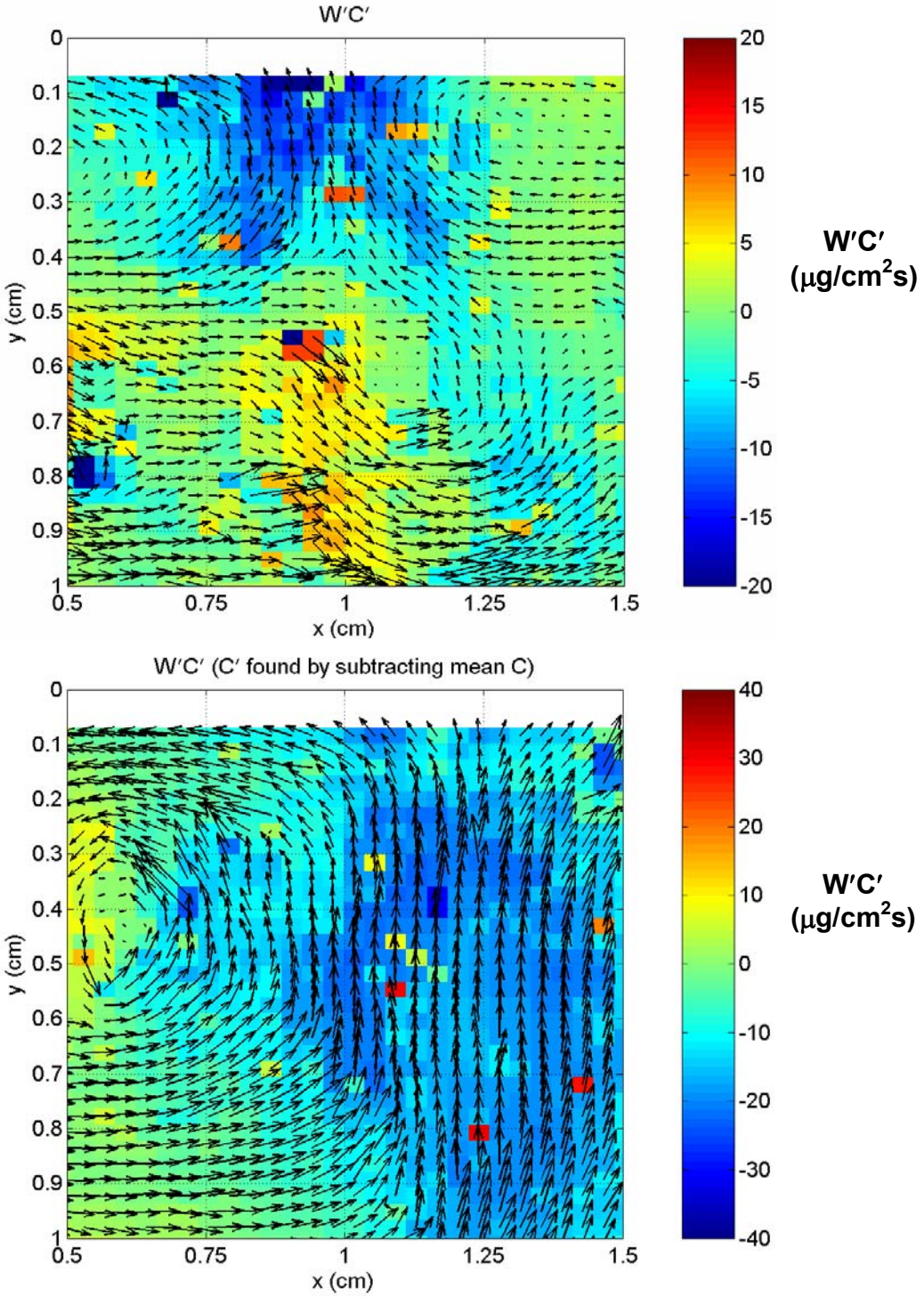

Figure 16. Instantaneous mass flux and velocity fields showing surface renewal events in which upward-moving fluid thins the CBL, increasing the rate of molecular diffusion across the interface. Negative mass flux indicates mass flux into the fluid.

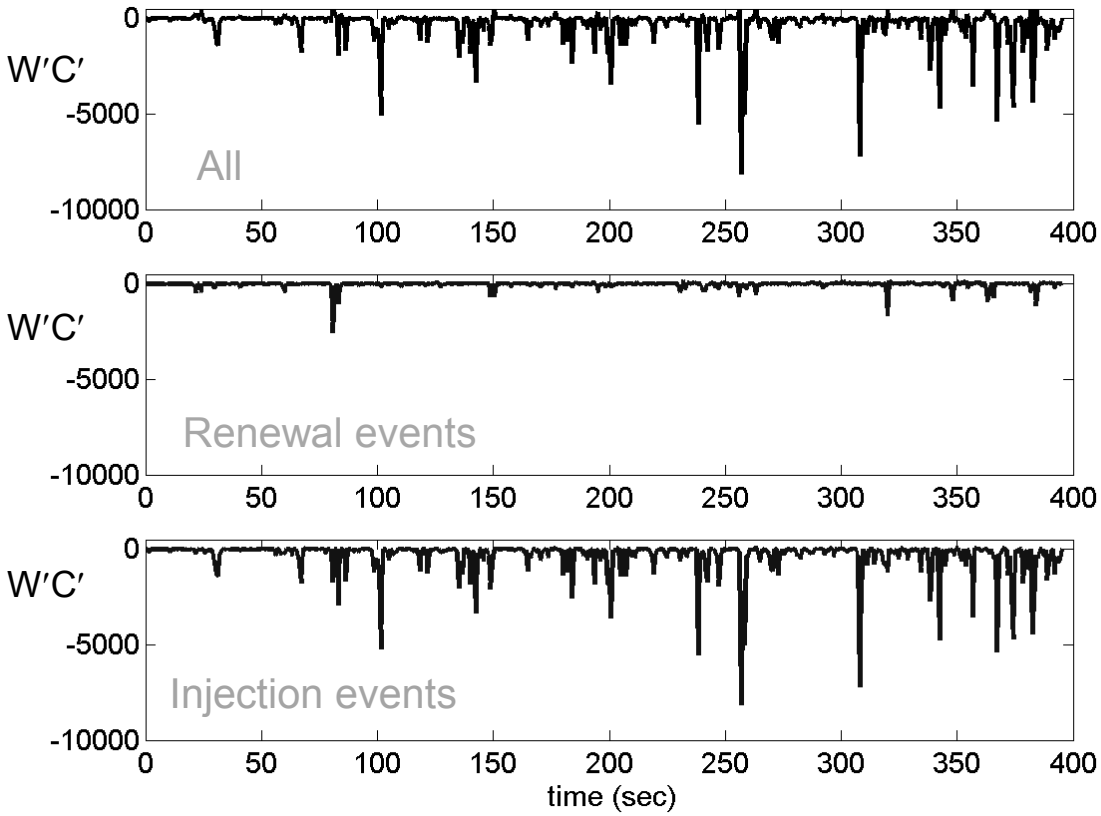

Figure 17. **(a)** Time series of instantaneous mass flux, horizontally averaged across a line parallel to the free surface at the smallest depth measured. **(b)** and **(c)** show this time series conditional on the sign of W'.

Is the dominance of downwelling mass flux due simply to a predominance of downwelling flow? We find this is not true by examining the skewness of the distribution of W' for the entire dataset and the distribution of W' conditional on mass flux into the fluid. The results of this analysis, seen in Table 5, show that downwellings are slightly more common than upwellings in this flow overall, but are much more common during periods of mass flux into the water.

Table 5. The distributions of W' and mass flux conditional on W' show that the predominance of mass flux during downwelling events seen in Figure 17 are not due to a predominance of downwelling flow in general. Recall positive skewness indicates a distribution peaked "skewed" to the left of a normal distribution.

	Mean	**Median**	**Skewness**
W'	-0.04	-0.09	0.61
$W' \mid W'C' < 0$	-0.026	-0.118	1.234

Are these mass injections events really caused by turbulence? Surface waves may be responsible, so we test this by looking for correlations between the time series of the horizontal average of W'C'at the free surface and the time series of dh/dt, where h is the free surface height. Since a correlation between the two may be time delayed, we calculate the correlation with a delay of 0, 0.8, and -0.8 seconds. None of these time series show a correlation significantly different than zero.

Still considering turbulence a "red herring," the injection events may be caused by density effects. If the fluid in the CBL is more dense than that in the bulk, it will descend in plunging fingers that resemble the injection events we see. The density difference could be thermal, due to evaporative cooling of the surface, or chemical, from the increase in dissolved CO_2. The chemical effect on density is negligible – the highest measured CO_2 concentration of 300 mg/L corresponds to a density change of 0.03 %. Herlina and Jirka (2004) test the thermal effects by running an experiment with and without turbulence generation, and find that injections cease when turbulence does. Furthermore, Schladow *et al.* (2002) specifically study plunging plumes from a cooled surface layer, and to obtain a gas transfer velocity of K_{600} = 1.07 cm/hr they

must create a temperature difference of 18˚C between the surface and bulk (a density change of 0.2 %). Thus mass transfer in our system is not dominated by thermal effects.

3.8 Analysis

It is believable that mass injection events are the dominant mechanism of turbulent mass transfer across an interface, despite the fact that until now most attention has been paid to surface renewal events. Several other systems serve as strong analogies for this type of phenomenon. The turbulent atmospheric boundary layer is heated from below, by longwave radiation from the Earth's surface. The scalar heat is transferred from the thermal boundary layer into the bulk of the troposphere in rising plumes of hot air with distinct sharp edges called thermals. These events are much more compact than the more diffuse downwelling that serves to balance the mass lost in the rising plume, so much so that gliders can catch a thermal to gain altitude but don't have to worry about being pulled downwards in analogous sinkholes. Recent studies of the thermohaline circulation in the world's oceans shows that the downwelling areas in polar regions where salty, cold water plunges into the abyssal ocean are relatively small - on the order of 10 km in diameter - while the deep water rises to replace it in an extremely diffuse manner throughout the entire remainder of the ocean (private communication, Jacob Berg Jörgensen). Langmuir cells on the surface of lakes and oceans exhibit a strong downwelling at the convergence of two eddies, and an upwelling that is more diffuse (Goldman and Horne 1983). Fortescue and Pearson, in their model of surface renewal eddies, state that "…the absorbed gas is carried into the bulk of the fluid largely by the layers of "surface" fluid that plunge downwards near the edge of the eddy." This points out that surface renewal and surface injection are really two sides of the same coin, both

processes caused by turbulent eddies interacting with the CBL. Thus any parameterization of gas transfer based on the number, size, and strength of eddies approaching the free surface could be successful, even if the modelers' understanding of the fundamental physics by which eddies affect gas transfer does not include the existence and possible dominance of injections.

The observed dominance of injection events may be due to the scale and location of our measurements. It is possible that higher resolution measurements closer to the free surface could show strong surface renewal events, showing that the effect of upwellings is less diffuse either for small eddies or very close to the free surface. However, even if surface renewal events were as diffuse as possible, so that they couldn't even be identified as events but were rather just a slow movement of low [CO_2] bulk fluid rising to replace the fluid moving downwards in injection events, the existing parameterizations would still hold, since they are based on the frequency and strength of eddies approaching the surface, and not the details of near-surface physics unknown when the model was constructed. Our observations of near surface physics will hopefully make future models more accurate.

Recent studies of gas transfer across an air-water interface by Herlina and Jirka (2004) and Takehara and Etoh (2002) report injection events like those discussed here. Herlina and Jirka interpret these events as evidence for the surface renewal theory, which further emphasizes that both upwelling and downwelling events are part of the same process, namely the interaction of eddies with the free surface. However, this work is the first to quantitatively compare the influence of these related processes, showing that the downwelling events dominate gas transfer from an instantaneous and local perspective.

3.9 Extensions

Future experiments will attempt to reproduce and confirm the results reported here, with increased quality on a number of fronts as discussed in the text. After these improvements have been made, further experiments will investigate the effect of Reynolds number and a thin surfactant layer on the near-surface physics of gas transfer.

Potential areas for related research include the small scale physics of turbulent flow in mass transfer at a solid flat surface (analogous to thermals in the atmospheric boundary layer), or around a model of any aquatic organism whose respiration depends on gas transfer at its surface. Examples include corals and macrophytes. Of great importance to the air-sea flux of CO_2 is bubble-mediated gas transfer (Thorpe *et al.* 2003), we could directly measure the physics of gas transfer by bubbles entrained by plunging round or planar jets, or even models of breaking waves. Air-sea flux in the polar regions is likely effected by ice patches floating on the surface. Our technique could work to measure the effects underneath a partially ice-covered surface. Fabrice Veron is leading a group currently investigating the effects of rain on air-sea gas transfer; this technique could be of use to such efforts.

APPENDIX A

FINDING CO_2 CONCENTRATION FROM PH

Our goal is to find the total amount of carbon to have entered the system, called C_T, which comes in several species:

C_T = total dissolved carbon = $[CO_2(aq)]+[H_2CO_3]+ [HCO_3^-]+[CO_3^{--}]$

$[CO_2(aq)] + [H_2CO_3]$ are considered together as $[H_2CO_3^*]$

C_T = total dissolved carbon = $[CO_2(aq)] + [H_2CO_3] + [HCO_3^-] + [CO_3^{--}]$

The different species exist in fractions α_i which are a function of activity constants and pH:

$$[H_2CO_3^*] = \alpha_0 C_T$$

$$[HCO_3^-] = \alpha_1 C_T$$

$$[CO_3^{--}] = \alpha_2 C_T$$

The Electroneutrality, or charge balance equation gives

$$[H^+] + [Na^+] = [HCO_3^-] + 2[CO_3^{--}] + [OH^-] + [Cl^-]$$

Substituting for $[HCO_3^-]$ and $[CO_3^{--}]$

$$[H^+] + [Na^+] = \alpha_1 C_T + 2\,\alpha_2\, C_T + [OH^-] + [Cl^-]$$

Solving for C_T

$$C_T = ([H^+] + [Na^+] - [OH^-] - [Cl^-]) / (\alpha_1 + 2\alpha_2); \text{ in mols/L}$$

It is interesting to note that α_0 does not appear in this equation, despite the fact that it is the largest fraction, ≈ 0.9, thus C_T is determined here from the concentrations of the two smaller species.

$[Na^+]$ and $[Cl^-]$ are known because we add NaCl to the tank in known amounts

$[H^+]$ is known from 10^{-pH}, while $[OH^-] = k_w/[H^+]$

The values of activity constants used here are pk1 = 6.35; pk2 = 10.33; pkw = 14; pkH = 1.5. As in the case of pH, the activity constants $k = 10^{-pk}$. They are corrected for ionic strength (known because the NaCl we add dominates all other ions) with the Debye Huckel law (Stumm and Morgan 1970).

APPENDIX B

FACILITY GEOMETRY

The experimental facility was retrofitted into the tank of Thomas Bourdel (http://milou.msc.cornell.edu/turb/jetarray.ps), described below.

A plexiglass octagonal tank (seen in figure 1) was sealed to the stainless steel orifice plate by compression from above onto an octagonal o-ring in a groove in the plate. An inner baffle could be added to give the desired symmetry constraint, but this was not used in these experiments. This is because it obscures viewing by the camera and reduces the number of jets from 16 to 9.

The tank is covered on the inside by black Vinyl Duct Tape (3M #3903) which has a matte finish and acts well as a dark background for imaging. The flow is driven by a 1.5 Horsepower 208 Volt pump (O.A. Smith type P), with flowrate set by a drive controller (Magnetek GPD 503).

As seen in figure 3, solenoid valves are plumbed in-line for each of the tubes leading to excurrent ports. All ports have inner diameter 0.90 cm.

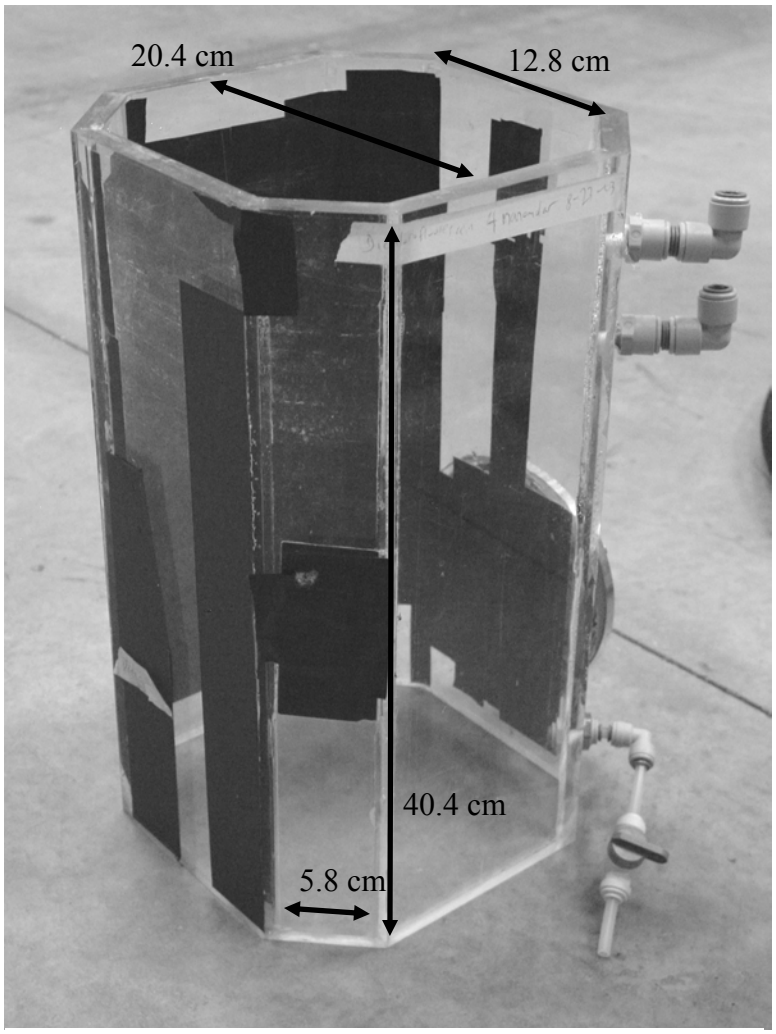

Figure 18. The octagonal tank, with dimensions. Note two bulkhead fittings for setting free surface height.

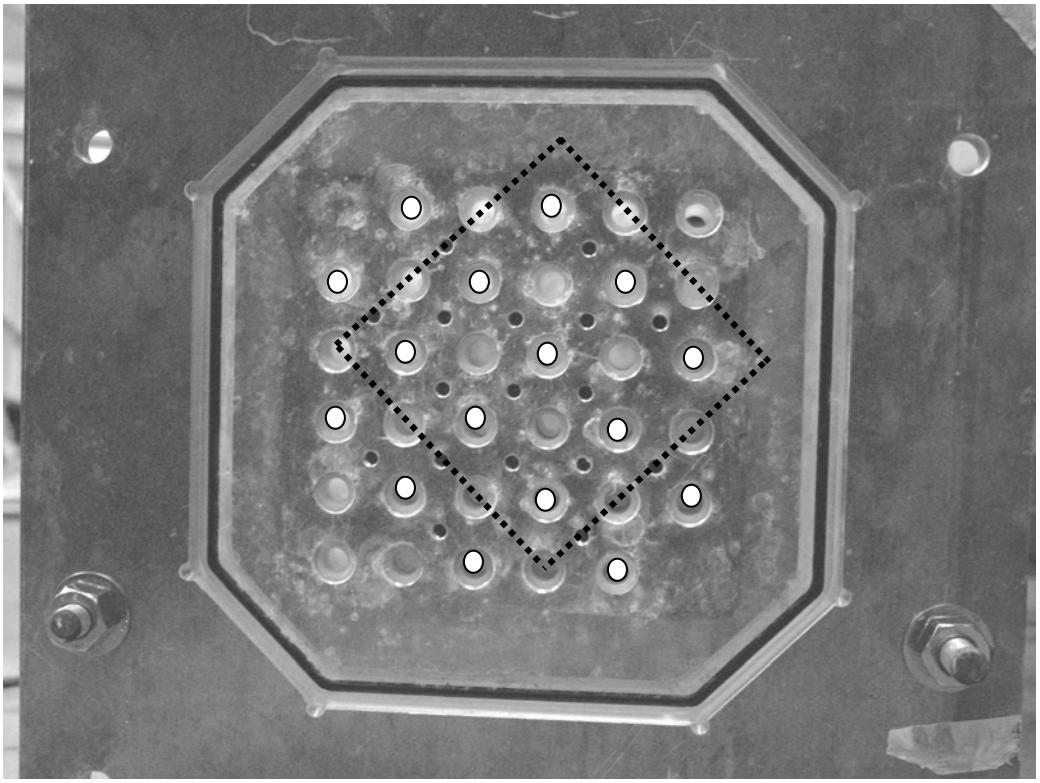

Figure 19. The orifice plane. Dashed line is footprint of rectangular inner baffle. Circles represent excurrent ports, squares are ports for draining/filling tank. All other ports are incurrent ports. Spacing between ports is 3.0 cm.

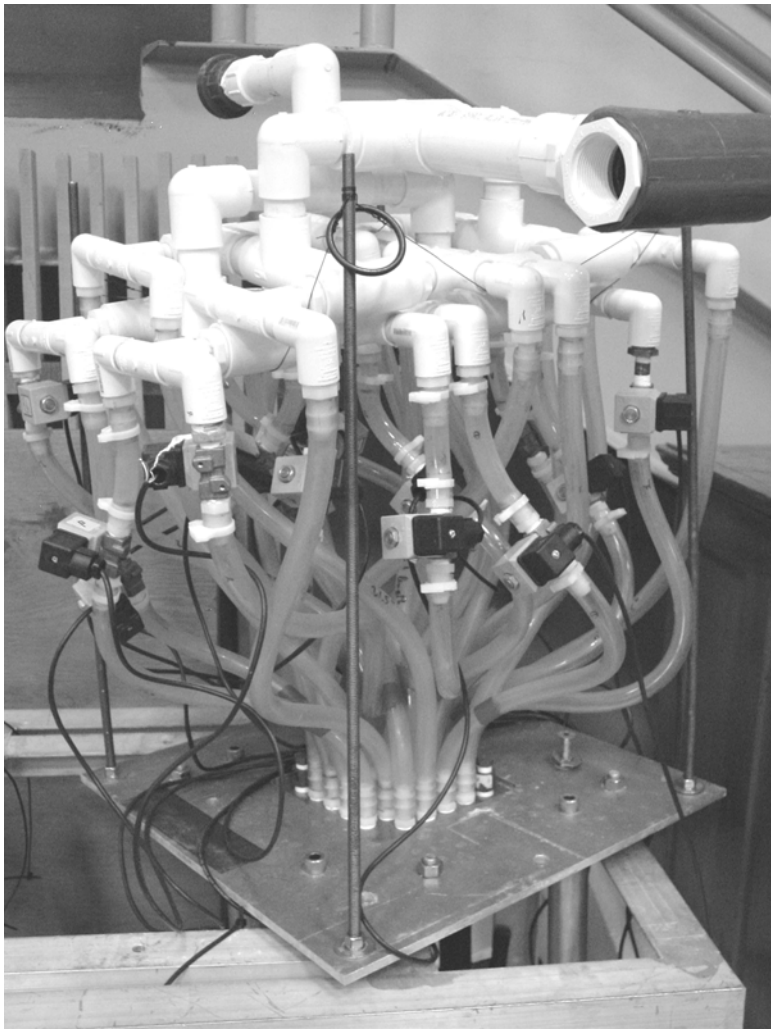

Figure 20. Synthetic jet manifold

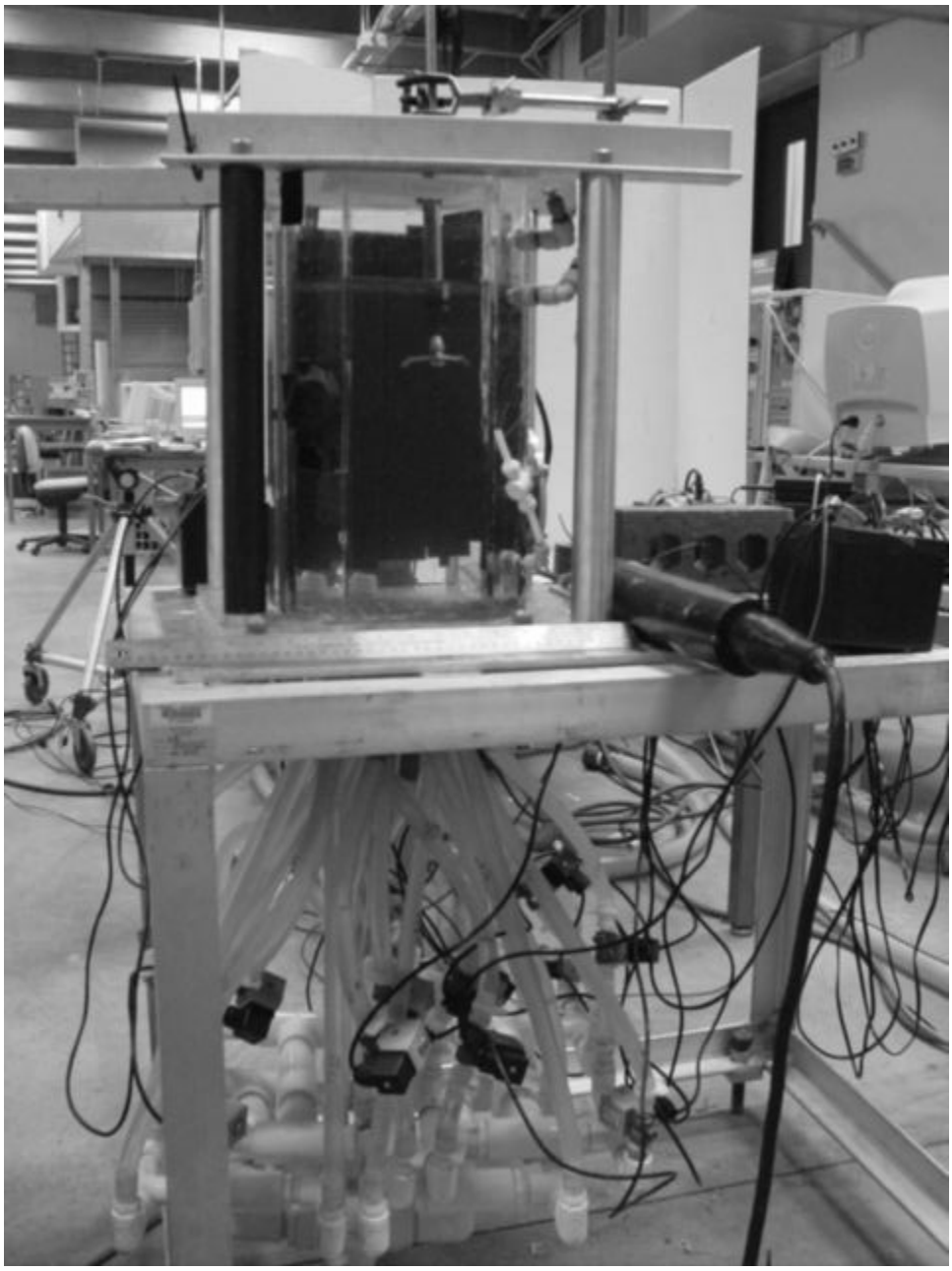

Figure 21. Assembled Experiment

REFERENCES

Asher W, Wanninkhof R (1998) Transient Tracers and Air-Sea Gas Transfer. *Journal of Geophysical Research* 103 (C8): 15939-15958

Asher W, Pankow J (1986) The interaction of mechanically generated turbulence and interfacial films with a liquid phase controlled gas/liquid transport process. *Tellus* 38B: 305-318

Asher W (1987) *An examination of the hydrodynamics governing a liquid-phase rate controlled gas/liquid mass transport process at clean and film-covered liquid surfaces* Ph.D. Thesis, Oregon Graduate Center with advisor James Pankow

Asher W, Jessup A T, Atmane M A (2004) Oceanic application of the active controlled flux technique for measuring air-sea transfer velocities of heat and gases *J. Geophys. Res.* 109

Banner ML, Peirson WL (1998) Tangential Stresses beneath Wind-Driven Air-Water Interface. *J. Fluid Mech*. 364: 115-145. As Cited in Siddiqui 2002

Brumley B, Jirka G (1987) Near-Surface Turbulence in a Grid-Stirred Tank *J. Fluid Mech.* 183: 235-263

Chu C, Jirka G (1992) Turbulent gas flux measurements below the air-water interface of a grid-stirred tank *Int. J. Heat Mass Transfer* 35(8): 1957-1968

Cowen EA, Monismith SG (1997) A hybrid digital particle tracking velocimetry technique. *Exp. Fluids* 22: 199-211.

Cowen EA, Chang K-A, Liao Q (2001) A Single-Camera Coupled PTV-LIF Technique *Exp. in Fluids* 31: 63-73

Dankwerts PV (1951) Significance of liquid-film coefficients in gas adsorption *Industrial and Engineering Chemistry* 43(6): 1460-1467

Doron P *et al.* (2001) Turbulence characteristics and dissipation estimates in the coastal ocean bottom boundary layer from PIV data. *Journal of Physical Oceanography* 31(8 part 1): 2108-2134

Efron B, Tibshirani R (1993) *An Introduction to the Bootstrap* Chapman & Hall

Fortescue GE, Pearson JRA (1967) On Gas absorption into a turbulent liquid *Chemical Engineering Science* 22**:** 1163-1176

Goldman C, Horne A (1983) *Limnology*, McGraw Hill

Hart, DP (2000) PIV Error Correction *Exp. Fluids* 29(1): 13-22

Herlina, Jirka GH (2004) Application of LIF to investigate gas transfer near the air-water interface in a grid-stirred tank *Exp. Fluids* 37: 341-349

Hiby JW, Braun D, Eickel KH (1967). Eine Fluoreszenzmethode zur Untersuchung des Stoffubergangs bei der Gasabsorption im Riesel-film. *Chemie Ing Techn* 39: 297-301. As cited in Münsterer and Jähne (1998).

Hwang W, Eaton J (2004) Creating homogeneous and isotropic turbulence without a mean flow *Exp. Fluids* 36: 444-454

Jähne B, Haußecker H (1998) Air-water gas exchange. *Annual Review of Fluid Mechanics* 30: 443-468

Komori S *et al* (1993) DNS of 3D open channel flow with zero-shear gas-liquid interface *Phys. Fluids A* 5:115

Kumar S, Gupta R, Banerjee S (1998) An experimental investigation of the characteristics of free-surface turbulence in channel flow. *Physics of Fluids* 10 (2): 437-456

Lamont JC, Scott DS (1970) An eddy cell model of mass transfer into the surface of a turbulent liquid *AIChE J* 16:513–519

McKenna S (2000) *Free-Surface Turbulence and Air-Water Gas Exchange* Ph.D. Thesis, Massachusetts Institute of Technology with advisor Wade McGillis

Münsterer T, Jähne B (1998) LIF measurements of concentration profiles in the aqueous mass boundary layer. *Exp. Fluids* 25: 190-196

Mydlarski L, Warhaft Z (1996) On the onset of high Reynolds number grid generated wind tunnel turbulence *J. Fluid Mech.* 320: 331-368

Pope SB (2000) *Turbulent Flows* Cambridge University Press

Schladow SG *et al.* (2002) Oxygen transfer across the air-water interface by natural convection in lakes. *Limnology and Oceanography* 47(5): 1394-1404

Siddiqui MHK *et al.* (2002) Turbulence Generated by Microscale Breaking Waves and its Influence on Air-Water Gas Transfer. In *Gas Transfer at Water Surfaces,* ed. Donelan *et al.* Geophysical Monograph 127, 2002, American Geophysical Union

Soli A L, Byrne R H (2002) CO_2 system hydration and dehydration kinetics and the equilibrium CO_2/H2CO3 ratio in aqueous NaCl solution *Marine Chemistry* 78(2-3): 65-73

Stumm W, Morgan J (1970) *Aquatic Chemistry.* Wiley Interscience

Takehara K, Etoh G (2002) A Direct Visualization Method of CO_2 Gas Transfer at Water Surface Driven by Wind Waves. In *Gas Transfer at Water Surfaces,* ed. Donelan *et al.* Geophysical Monograph 127, 2002, American Geophysical Union.

Tamburrino A, Gulliver J S (2002) Free-surface turbulence and mass transfer in a channel flow *AIChE J.* 48 (12): 2732-2743

Thorpe SA *et al.* (2003) Bubble clouds and Langmuir circulation: Observations and models *Journal of Physical Oceanography* 33(9): 2013

Villermaux E, Hopfinger E (1994) Periodically arranged co-flowing jets *J. Fluid Mech.* 263: 63-92